Lightweight Helmet with Rotating Permanent Magnets for Brain Injury Rehabilitation

Jessica Havas, Mosa Alzowelei, Michael Congdon, Tanya Wang, Ying Sun, Ph.D., Brian Silver, MD*
Biomedical Engineering, University of Rhode Island, 4 East Alumni Avenue, Kingston, RI 02881;
* Rhode Island Hospital, Providence, RI 02903. Correspondence email: yingsun@uri.edu

***Abstract*—This project is concerned with the development of a wearable transcranial magnetic therapeutic device that employs a mechanism of rotating permanent magnets. The device is intended for the enhancement of brain injury rehabilitation. Rare earth magnets are mechanically rotated to generate time-varying magnetic fields on specific injured areas of the brain. Each therapeutic probe consists of two neodymium disc magnets arranged in a concave position toward the brain and enclosed in a customized 3D-printed housing. The magnet holder is rotated with a DC motor controlled by a microprocessor and a pulse width modulator for the desirable rotational speed, timing, and treatment protocol. The components are integrated in a lightweight helmet suitable for frequent rehabilitation sessions over a prolonged period of time or for at-home use. The effectiveness of the low-level, mechanically varied magnetic field therapy will be further studied in future clinical investigations.**

Keywords—brain injury; rehabilitation; permanent magnet; wearable; rotation mechanism; transcranial magnetic stimulation; static magnetic field therapy

I. Introduction

Traumatic brain injuries and acquired brain injuries affect millions of people each year in the United States [1], and often leave devastating long-term symptoms. They may also cause temporary disabilities which require long-term rehabilitation therapy in order to overcome.

Transcranial magnetic stimulation (TMS) is a noninvasive therapy used to stimulate local regions of the brain. This method utilizes electrical currents generated in coils in order to induce magnetic fields of varying frequencies. These magnetic pulses with a strength on the order of 1 Tesla are then focused through specific placement on the head in order to polarize target areas of the brain. In recent years, TMS has been used to treat depression [2] and several neurodegenerative diseases including Parkinson's and Alzheimer's [3], with varying degrees of success. TMS has also been studied in patients with upper limb weakness following stroke with results suggesting possible benefits [4]. The effectiveness of transcranial magnetic stimulation (TMS) for brain injury rehabilitation has been demonstrated in several recent studies [5],[6]. Stimulating nerve cells in affected area via TMS may also aid in the rehabilitation of various stroke side effects other than just limb weakness. After a stroke occurs, many cognitive and motor abilities are affected. Memory and motor control in specific areas may be impaired or lost. Current TMS for stroke rehabilitation is preformed solely in a hospital setting for about 40 minutes. This procedure is also quite costly, thereby limiting availability to many patients. In this project an alternative lightweight helmet is developed to employ rotating permanent magnets for transcranial magnetic therapy over a prolonged period of application time and suitable for at-home use.

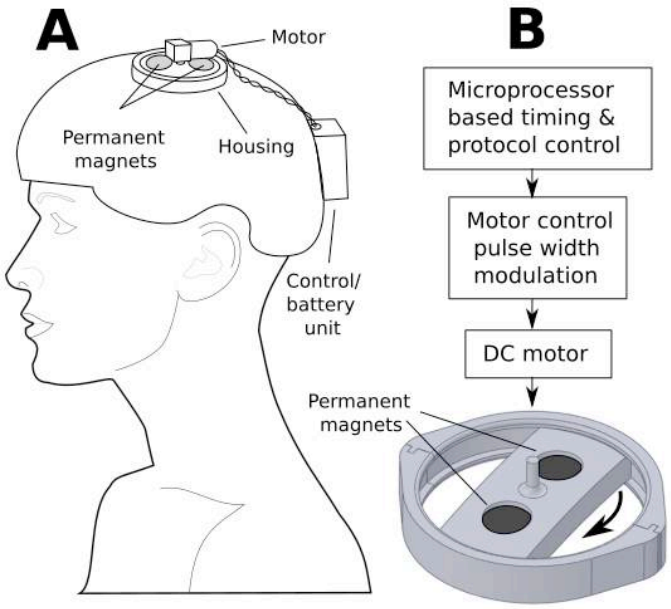

Fig. 1. (A) Schematic diagram showing the design of a wearable transcranial magnetic therapeutic device; (B) block diagram for the control of the rotating disc magnets mounted in a customized housing .

II. Methods

A. Mounting Mechanism for Disc Permanent Magnets

In contrast to a previous project using a sliding mechanism [7], the present project employs a rotational mechanism aiming at a faster and continuous circular motion. As shown in Fig. 1A, a magnetic therapeutic probe is positioned on the head with the support of a lightweight helmet. The placement of the therapeutic probe in the helmet must be flexible in order to target a specific injury area of the brain. Frequently targeted locations include the frontal lobe, the temporal lobe, parietal lobe, and occipital lobe. The two magnet discs are inserted into a concave holder toward the head for a better focus. The holder is fitted to a circular housing that supports a rotational motion.

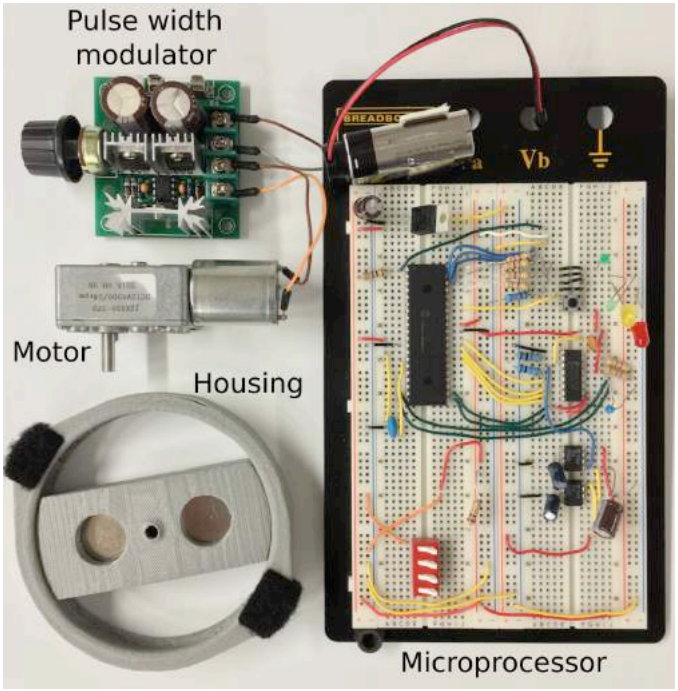

Fig. 2. Key components of the prototype including a housing for the disc magnets, a DC motor, a pulse width modulator for adjusting the motor speed, and a microprocessor for timing and protocol controls.

B. Control Unit

Fig. 1B shows the block diagram of the embedded control unit that uses a microprocessor to control the timing and the therapeutic protocol. The magnets are rotated by use of a DC motor. A pulse width modulator controls the speed of the motor.

III. Results

As shown in Fig. 2, the mounting holder and housing were designed with SolidWorks (Waltham, MA) and 3D-printed in ABS plastic by using a MakerBot Replicator 2X (Brooklyn, NY). The chosen permanent magnet was a N52 neodymium disc of 1" in diameter and 1/4" in thickness. The magnetic flux density normal to the surface was 0.33 T at the center of the disc, and 0.52 T on the perimeter. The holder was continuously rotated by use of a 12V DC motor (Model JSX330-370, Dmiotech) with a rated torque of 4 Kg•cm, a gear-down ratio of 330:1, and a maximum no-load speed of 24 rpm.

The control unit was developed around a PIC18F4525 microprocessor by using an ICD3 in-circuit programmer and the MPLab Integrated Development Environment (Microchip, Chandler, AZ). The electronics were initially developed on a breadboard and will be converted to a printed circuit board for better packaging. The electronics and the DC motor were powered by use of two 9V batteries to achieve a maximum voltage of 18 V.

IV. Discussion

This study has successfully resulted in a prototype of a battery-powered, wearable device for transcranial magnetic therapy. The magnetic flux density from the permanent magnets used in this project is about 1/3 T and the frequency of the mechanical rotation is about 2.5 Hz. Thus, the achievable magnetic flux change is about an order magnitude less than that of the transcranial magnetic stimulation (TMS), which has a magnetic flux density around 1 T and a pulse frequency between 1 Hz and 25 Hz. Nevertheless, the main advantage of this device is its low cost and wearability, allowing for frequent sessions of brain injury rehabilitation over an extended period of time.

Static magnetic field (SMF) therapy using permanent magnets has been used by people worldwide for self-care for may years; however, its healing mechanisms, dosing parameters, and treatment regimens have not yet been well defined [8],[9]. The proposed device of trancranial magnetic therapy falls into a paradigm between TMS and SMF. The rotating permanent magnets create a dynamic magnetic field; however, its strength is not likely to reach the level of inducing action potentials in neurons.

This project has contributed to a proof-of-concept prototype outlining the engineering solutions and the performance indices of the resulting magnetic flux density and frequency. For future work, the prototype will be further improved to be used in clinical studies on the effectiveness of the transcranial magnet therapy for long-term rehabilitation of brain injuries.

Acknowledgement

The authors would like to acknowledge the grant support from the 2015-2016 Undergraduate Research Initiative Awards of the University of Rhode Island.

References

[1] Brian Injury Society of America. *Brian Injury Facts*, http://www.biausa.org/LiteratureRetrieve.aspx?ID=104992, retrieved Feb. 2016.

[2] Levkovitz, Y., et al. Deep transcranial magnetic stimulation over the prefrontal cortex: evaluation of antidepressant and cognitive effects in depressive patients. *Brain Stimul*., vol. 2(4), pp.188-200, 2009.

[3] Anderkova, L., and I. Rektorova. Cognitive effects of repetitive transcranial magnetic stimulation in patients with neurodegenerative diseases - clinician's perspective. *J. Neurol Sci*., vol. 339(1-2), pp. 15-25, 2014.

[4] Corti, M., C. Patten, and W. Triggs. Repetitive transcranial magnetic stimulation of motor cortex after stroke: a focused review. *Am. J. Phys. Med. Rehabil*., vol. 91(3), pp. 254-270, 2012.

[5] Sack, A. T., et al. Optimizing functional accuracy of TMS in cognitive studies: a comparison of methods. *J. Cogn. Neurosci*., vol. 21(2), pp. 207-221, 2009.

[6] Levkovitz, Y., et al. A randomized controlled feasibility and safety study of deep transcranial magnetic stimulation. *Clin. Neurophysiol*., vol. 118(12), pp. 2730-2744, 2007.

[7] Davis, R., S. Dezrick, Z. Jacobson, T. Wang, Y. Sun Y, B. Silver. Static magnetic field helmet for brain injury rehabilitation. 41st Northeast Bioengineering Conference, Troy, NY, April 17-19, 2015.

[8] Colbert , A. P., et al. Static magnetic field therapy: A critical review of treatment parameters. *Evid. Based. Complement. Alternat. Med.*, vol. 6(2), pp. 133–139, 2009.

[9] Markov, M. S. Magnetic field therapy: a review. Electromagn. Biol. Med., vol. 26(1), pp. 1-23, 2007.

Collision Avoidance and Adaptations to Ride-On Cars for Children with Mobility Impairments

Cara Nunez, Katie Brown, Zachary Campo, Coral Hines,* Sandra Maliangos,* and Ying Sun, Ph.D.
Department of Electrical, Computer and Biomedical Engineering and *Department of Physical Therapy
University of Rhode Island, 4 East Alumni Avenue, Kingston, RI 02881

***Abstract*— Children with physical disabilities exhibit less independence and freedom than other children. To solve this problem, ride-on cars were adapted for children with limited mobility, empowering them to interact better with their peers and increase their confidence. A support system made of polyvinyl chloride (PVC) pipes and harness was added to improve the overall safety of the car and maintain the children in an upright position. The controls of the cars were modified in order to accommodate the child's specific needs. Additionally, a collision avoidance system created with ultrasonic sensors, embedded C programming, and relays reduced the risk of collision with surrounding objects. A prototype was developed and used as a guidance for adapting additional cars for children with mobility impairments living in the community. This prototype offered the potential for commercialization of the product for a broader market.**

Keywords*— *children with mobility impairments; ride-on cars; adaptation; polyvinyl chloride pipe; collision avoidance

I. Introduction

Cerebral palsy, the most prevalent mobility impairment condition among children, affects approximately 3.1 out of every 1,000 children in the United States. 10,000 infants and children are diagnosed with this condition each year. Children with cerebral palsy and children with other mobility impairments face everyday challenges such as walking and coordinating voluntary muscle movements. In order to solve this problem without expensive automatic wheelchairs, which can cost upwards of thousands of dollars, ride-on cars are being adapted to fit children's needs. The study by Huang et al. [1] concluded that "modified toy cars have serious potential to be a fun and functional power mobility option for children with special needs." Deitz et al. [2] showed that the use of a powered mobility device for children with severe motor impairments and developmental delay may increase self-initiated movement occurrences during free play.

The commercially available ride-on cars typically require that children operate a steering wheel and foot pedal simultaneously which presents a nearly impossible task for children with cerebral palsy and other mobility impairments. Thus, a multidisciplinary team was formed at the University of Rhode Island consisting of students from biomedical engineering and physical therapy to engage in a ride-on car adaptation project. The team developed a prototype of a modified ride-on car for children with mobility impairments that includes an alternative control system, additional safety features, and a collision avoidance system employing ultrasonic sensors. The adapted car improved the child's mobility as well as encourage physical therapy exercises.

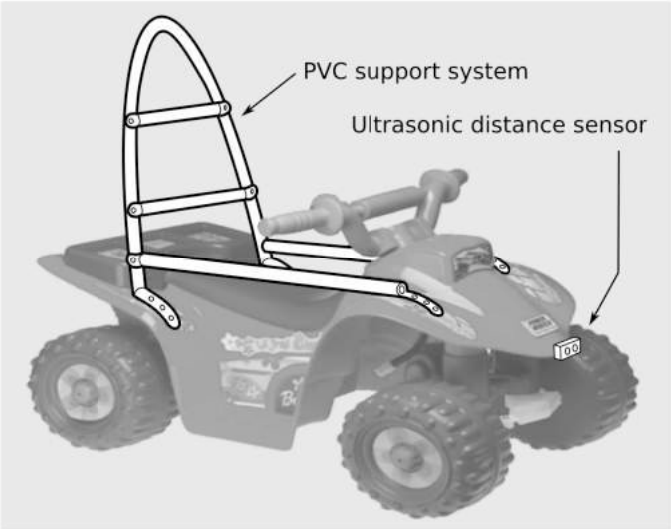

Fig. 1. Adaptations to the ride-on cars including a support system made of PVC pipes and a collision avoidance system based on a ultrasonic distance sensor.

Based on patient measurements, disability, intended rehabilitation exercises, and parent recommendations, the adaptions of additional ride-on cars continue.

II. Methods

A. Support Design

The first step in adapting the ride-on car was creating a special support system for the child. Safety features were added to the car by molding and attaching polyvinyl chloride (PVC) pipes. Using a heat gun, PVC pipes were shaped optimally to provide ergonomic and therapeutic supports. The heat-molding technique was also used to provide secured connections of the PVC frame to car chassis. Appropriate paddings and cushions were attached for comfort. The support system was intended to confine the child within the car and gave guardians the ability to easily reposition the car.

B. Electrical Design

The electrical system of the car was rewired to replace the original control mechanism with an adaptive switch that was deemed suitable for the specific child [3]. To implement this modification, an 1/8 inch audio jack was soldered in parallel with the original accelerator. This audio jack is an industrial standard, which makes the design universal and compatible with commercially available adaptive switches. As the children strengthens their mobility impairment, they may no longer require the added adaptive switch. If this occurs, the

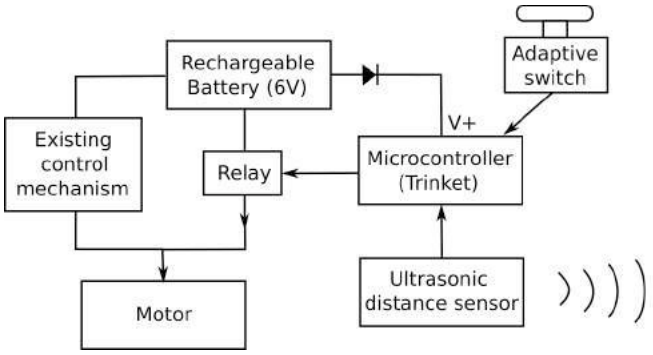

Fig. 2. Schematic of the embedded control system with collision avoidance capability based on an ultrasonic distance sensor.

adaptive switching system could be easily removed or changed.

A collision avoidance system was also developed to provide an additional safety feature. An ultrasonic distance sensor module (HC-SR04) was chosen, which provides a range of 2 cm to 4 m with an accuracy of 3 mm. As shown in Fig. 2, the distance sensor was under the control of a microcontroller (Adafruit Trinket – Mini). The electronics required a DC power (V+) of 5 V, which came from the 6V car battery via a diode. If the car battery was 12V, a 5V voltage regulator was used.

III. Results

The initial experience of adapting five ride-on cars for specific children was very positive. The PVC heat-molding method proved to be very effective and saved the cost of using PVC pipe fittings and joint adhesive. For example, the cost for 1-inch PVC pipe was $0.45 per feet. A 1-inch T-connector was US$0.88 and an 8-oz PVC cement was $5. In addition, the main support structure based on a single bended PVC pipe was stronger than an assembly of multiple straight PVC pipe segments with fittings.

The Trinket was programmed in the embedded C language with the Arduino IDE tool. The on-chip pulse width modulation (PWM) support of the Trinket was programmed to probe the forward distance periodically by sending pulses to the distance sensor. As shown in Fig. 3, in response to the probing pulse, the distance sensor returned a square wave with a duration proportional to the distance. Should the distance sensor detect an object within a pre-determined safety distance (for example, 1/2 m), the adaptive switch control was overwritten and the car was stop. As part of the cost analysis, the Adafruit Trinket costed $7 and the ultrasonic distance sensor also costed $7.

IV. Discussion

This project was based off several previous and on-going projects of adapting ride-on cars for children with disabilities, such as the *Go Baby Go* project at the University of Delaware [4]. Our experiences have contributed to the design aspects in terms of the PVC heat-molding technique, the embedded control, and the ultrasonic collision avoidance system. These

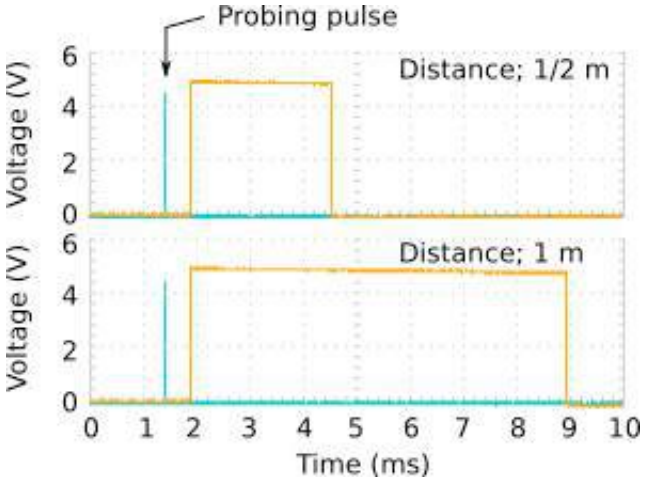

Fig. 3. Timing of the probing pulse and the ranging signal from the ultrasonic distance sensor for an object at 1/2 m away (top) and 1 m away (bottom).

techniques should improve the cost-effectiveness and safety of the adaptive ride-on cars.

Based on the initial prototype, five more cars were adapted for specific children with varying disabilities. The adaptions of these five cars were different in certain aspects depending on the specific needs of the children. For example, to best help a child suffering from cerebral palsy who cannot control both a foot pedal for power and a steering wheel simultaneously, a joystick was implemented to combine power and steering into one instrument. Increased safety features were added in addition to the PVC support and collision avoidance device, such as harnesses to restrict excessive movement and flailing. Depending on the needs of the child and the family, parental override controls were also being considered. The parental controls would allow the parents to stop the cars and override the child controlling the cars in the case of an emergency. Future work also aims to commercialize this idea, which could be packaged as a ride-on car adaptation kit.

Acknowledgment

This project was supported in part by an grant from the 2015-2016 Undergraduate Research Initiative Awards program of the Division of Research & Economic Development, University of Rhode Island.

References

[1] Huang, H., C. B. Ragonesi , T. Stoner, T., Peffley and J. C. Galloway . “Modified toy cars for mobility and socialization: case report of a child with cerebral palsy,” Pediatric Physical Therapy, vol. 26(1), pp. 76-84, 2014.

[2] Deitz, J., Y. Swinth, O. White. “Powered mobility and preschoolers with complex developmental delays. American Journal of Occupational Therapy, v. 56, pp. 86-96, 2002.

[3] Crisco, J. J. et al. “Design and kinematic evaluation of a novel joint-specific play controller: Application for wrist and forearm therapy.” Physical Therapy, vol. 95(7), pp. 1061–1066, 2015.

[4] Patterson, C. "Guide for modified assembly: Lightning McQueen." <http://www.udel.edu/PT/AboutUs/People/Galloway/GoBabyGoManual McQueenStepByStep.pdf>, Dec. 2015.

Undergraduate Design Project on a Stove Barrier for Burn Prevention in Kenya

Sakoun Phommavongsa, Robert Valenti, Tracy Waweru, Shahla Yekta,* and Ying Sun
Department of Electrical, Computer and Biomedical Engineering, University of Rhode Island, 4 East Alumni Avenue, Kingston, RI 02881, USA; *Department of of Plastic and Reconstructive Surgery, University of Toronto, Toronto, ON, Canada. Correspondence email: shahla.yekta@utoronto.ca

***Abstract*—In the urban slums of Sub Saharan Africa, overcrowding and unsafe cooking stoves have caused serious burn injuries amongst children. This project aimed to help preventing fire-related burns of children residing in the urban slums of Kenya by creating a prototype stove barrier. The design considerations included effectiveness, cost, materials availability, ease of assembly and disassembly, manufacturability, and aesthetics. After several design iterations, a prototype based on aluminum frames and mesh panels was shown to be cost-effective and received positively in the initial field test.**

Keywords—burn prevention; stove barrier; Kenya

I. Introduction

Burns are a major global health issue in low- and middle-income countries (LMIC). There is an estimated 300,000 global burn deaths per year, with fire-related burns being the 6th leading cause of death for children ages 5 to 14 years old in LMICs [1]-[3]. A recent study has shown that burn injuries contribute significantly to morbidity in LMICs and may be increased by urbanization to Sub Saharan slums [4].

A typical household in the slums of Kenya lives in a single crowded space with cooking done on a portable coal or kerosene stove. Children accidentally in contact with a hot stove or cookware could be inflicted with serious burn injuries. A barrier that keeps the children away from the stove could be an effective safety measure. Previously, several prototypes of stove barriers, as shown in Fig. 1, were developed by the "Burn Prevention – Africa" program of the Division of Plastic and Reconstructive Surgery, University of Toronto [1]. While these designs satisfy certain aspects of the burn prevention purpose, limitations do exist in terms of cost, size, availability of local materials.

Thus, this undergraduate design project aims to optimize the design of a stove barrier for burn prevention in developing countries. The design considerations include effectiveness, cost, materials availability, manufacturability, ease for assembly and disassembly, and aesthetics. The prototype will be initially designed and developed in USA and then transferred to the local regions for manufacturing and commercialization. The targeted retail price should not exceed US$10. Additional design considerations pertaining to the crowded living space that the stove barrier will be used. Thus, the final product should be mobile, compact, easy to assemble and disassemble, and aesthetically pleasing to the eye.

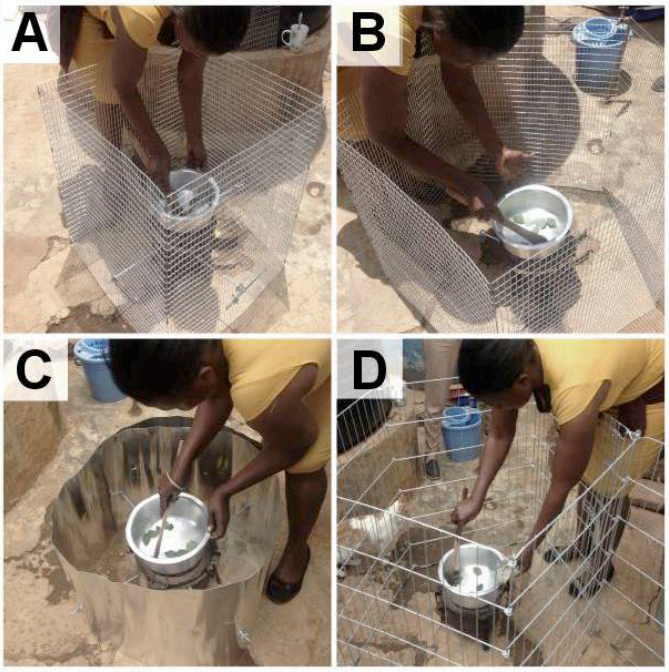

Fig. 1. Previously developed prototypes of the stove barrier for burn prevention using foldable hardware cloth panels of a 4-panel design (A) and a 5-panel design (B), a circular aluminum fence with struts connected to the stove (C), and a re-purposed dog cage (D). Courtesy of the "Burn Prevention – Africa" program of the University of Toronto [1].

II. Methods

A. Design Process

The design process began with constructing some prototypes based on the previous designs including the circular aluminum fence shown in Fig. 1C. In order to test the prototypes, a model of the coal stove typically used in Kenya was built. The model stove was adapted from a plastic bucket with a height of 12" and a diameter of 18". The main design issues were iteratively refined as follows:

1. For safety and effectiveness, the stove barrier must be able to stay upright firmly on its own.

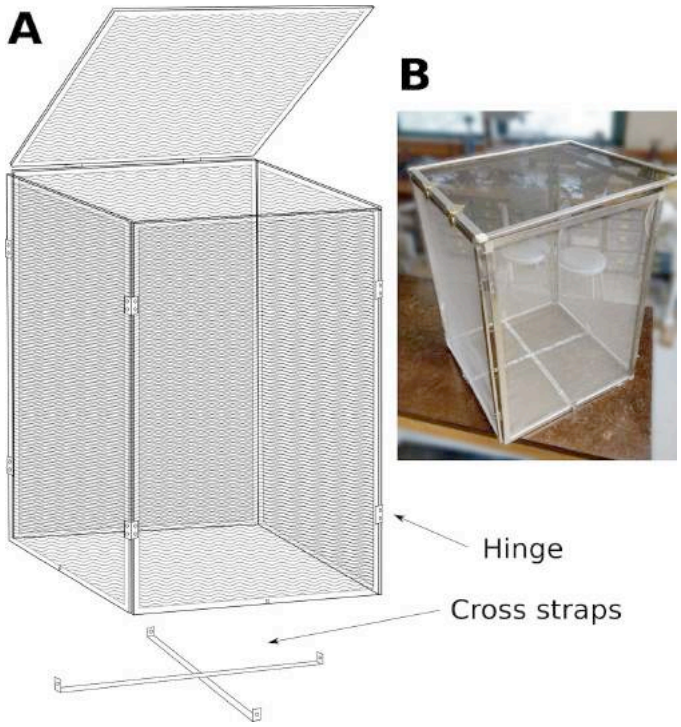

Fig. 2. (A) The design that meets almost all the required consists of 4 side panels with aluminum mesh, a top panel, and cross straps at the bottom. (B) A photograph of the prototype.

2. The stove barrier cannot be lifted or shifted easily relative to the stove placed in the center.
3. The barrier should be high enough to prevent children from climbing over, but not too high to make cooking difficult.
4. The footprint of the stove barrier should be minimized due to the crowdedness of the space, but not to the extent of compromising safety.
5. The barrier needs to be tucked away easily; thus, the ease of assembly/disassembly is an important consideration.
6. Availability and cost of the materials are importable considerations, while labor cost is relatively low in Africa.
7. See-through materials are favorable for a more aesthetic appearance and reducing the curiosity factor of the children.

B. The Design and Prototype

Fig. 2 shows the current and most efficient prototype that meets most of the requirements for an effective stove barrier. The four square panels of the barrier are comprised of 5/16" mill aluminum screen frame pieces originally meant for screen doors assembled into 1.5' x 2' rectangles. 5/16" plastic screen frame corners keep the aluminum mill pieces together. Aluminum mesh is tucked into the mill framing using rubber spline, completing the panel design. Panels are connected via two sets of hinges on the panels length-wise, allowing the stove fence to fold in on itself for easy storage and mobility. The bottom of the stove fence utilizes two metal straps running adjacent to one another across the bottom for additional stability. Stoves that sit upon the straps weigh down the fence so that children may not lift or shift the barrier. An additional panel with 1.5' x 1.5' dimensions folds over the top of the stove so that children may not reach inside. The cover swivels on a hinge that rotates 270 degrees backwards to keep it flush to the frame when not in use.

III. Results

The initial feedback was received from Kenya through the "Burn Prevention – Africa" team of the University of Toronto. The prototype developed in this project was considered favorably by the locals of Kibera, Kenya. The aluminum frame and aluminum mesh panels are aesthetically pleasing, and the see-through mesh removes the curiosity liability. The materials are lightweight and provide good mobility. Metal cross straps at the bottom enhance rigidity of the assembly. Placing a stove upon the straps helps to keep the barrier in place. Unfastening the metal straps makes the barrier foldable for storage. The addition of a lid on this variant is very well received by the locals, as it secures the top of the stove and also allows air to escape. Drawbacks to this model include the strap design, and the lack of availability of aluminum mesh in Kenya.

IV. Discussion

This project was concerned with a global health issue. A prototype stove barrier was developed that encloses a coal or kerosene stove for preventing burn injuries of children in Africa. The design consisted of meshed aluminum side frames, a top lid, and bottom cross straps for structural rigidity. The design process provided real-world experiences pertaining to effectiveness, feasibility, safety, product appearance, manufacturability, and market potential. The availability of materials in Kenya and their local costs were issues that required a significant amount of international coordination and communication. Market potential and commercialization also affected the design critically, as the overall cost was not to exceed $10 in an effort to maximize affordability. For future work, the cost and materials availability constraints have not yet been met and require further development and improvements.

Acknowledgment

The authors would like to acknowledge the grant support from the 2015-2016 Undergraduate Research Initiative Awards program of the University of Rhode Island.

References

[1] Division of Plastic and Reconstructive Surgery. University of Toronto. Burn Prevention – Africa. https://www.uoftplasticsurgery.ca/donate/case-studies/burn-prevention-africa/, Feb. 2016.

[2] Jugmohan, B., J. Loveland, L. Doedens, R. L. Moore, A. Welthagen, and C. J. Westgarth-Taylor. Mortality in paediatric burns victims: A retrospective review from 2009 to 2012 in a single centre. *South African Medical Journal*, vol. 106(2), pp. 189-192, 2016.

[3] Albertyn, R., S. W. Bickler, and H. Rode. Paediatric burn injuries in Sub Saharan Africa – an overview. *Burns*, vol. 32(5), pp. 605-612, 2006.

[4] Wong, J. M., et al. Sustained high incidence of injuries from burns in a densely populated urban slum in Kenya: an emerging public health priority. *Burns*, vol. 40(6), pp. 1194-200, 2014.

Design of a 3D Aerophilic Tissue Culture System with an Aerosolized Powder Insufflator

Analicia Behnke, Katherine Noonan, Nastasja Rittling, Samantha Meenach,* Ph.D., and Ying Sun, Ph.D.
University of Rhode Island, Department of Electrical, Computer, and Biomedical Engineering, *Department of Chemical Engineering, Kingston, RI 02881. Correspondence email: Prof. Meenach <smeenach@uri.edu>

***Abstract*— This project aims at developing a customized *in vitro* experimental system for testing mannitol, a cancer therapy excipient. In order to grow aerophilic lung tumor spheroids, micro-molds were designed to create 3D petri dishes made of alginate gel. Computer-aided design and 3D printing technology were utilized to create a plastic mold for generating flexible silicone molds, which then produced the desirable alginate scaffoldings. An insufflator was also designed for hand injection of mannitol powder onto a 6-well plate via a syringe. Based on testing with colored powders, a cone-shaped disperser inside the insufflator effectively improved the uniformity of the injected powder distribution. The project has resulted in a useful platform for designing components of a 3D tissue culture system with appropriate materials.**

Keywords—aerophilic tissue; lung tumor spheroid; aerosolized powder; insufflator; 3D printing; silicone rubber mold; alginate gel

I. Introduction

Pulmonary inhalation of chemotherapeutic drugs for lung cancer treatments are available in the form of aerosolized powders, which are advantageous over many other treatments due to their ability to effectively target regions deep within the lungs. A cell culture system can provide a useful platform for studying the effects of aerosolized chemotherapy drugs *in vitro*. Due to the aerophilic nature of the lung tumor cells, an effective tissue culture system has specific considerations that may require customized design. The experimental setting in this study is designed to grow 3D tumor cell spheroids in an alginate scaffold, which rest on a semi-permeable membrane in contact with nourishing cell media. The powder drug is applied with an insufflator and the sizes of the growing spheroids are measured with high-throughput image analysis software. For this project, the first objective is to create a silicone mold of a 3D petri dish specific to the size of a 6-well plate and corresponding Transwell®. The silicone mold will be used to hold the alginate gel, which is then positioned into the Transwell® and will be home to the growing spheroid cells. The second objective is to create a multipurpose spray system that will uniformly spray the spheroids with the aerosolized powder and cover each Transwell® to eliminate cross contamination when spraying the spheroids. The engineering components of this project include materials, methods, and mechanical designs for making the system more efficient, cost-effective, and easy to use.

II. Methods

A. Creating the Mold for Alginate Scaffolding

A customized alginate scaffolding to fit into a Transwell® of a 6-well plate was designed. The general shape of the scaffolding was modeled after a 3D Petri Dish® product from Microtissues for a 12-well plate containing a 5x7 array of spherical recesses and a rectangular geometry. The new design improved the efficiency by maximizing its area in the Transwell®. Using SolidWorks® (Waltham, MA), the inverse of the mold was created and then 3D printed with ABS plastic by using a MakerBot Replicator 2X® (Brooklyn, NY). The diameter of the inverse mold was 0.94 in. Testing the spheroid growth process with different array geometries in the lab, it was determined that a 7x7 array yielded the most effective spheroid growth. In addition, each corner recess of the micro-mold was removed to provide more successful placement into the Transwell® and leaves the area for 45 recesses for the cells to grow in, which was 10 more than the current method. The 3D-printed ABS plastic was smoothed with acetone to reduce surface roughness due to the resolution limitation of the 3D printer. Then the plastic inverse mold was used to create a silicone rubber mold. After 8 hours of curing, the silicone rubber mold was ready and used to create the alginate scaffolding for cell culture. The resulting scaffoldings were tested for culturing cellular spheroids.

B. Creating the Method for Powder Dispersion

The study of the aerosolized cancer therapy requires an effective and efficient method for administering the chemotherapeutic powder drug in a uniform manner and with minimal spillover to the neighboring Transwells®. In previous trials, the powder was applied with a commercially available insufflator (Penn-Century, Wyndmoor, PA) over each individual Transwell®. In this study a standard medical 3 mL syringe attached to 2 in. blunt tipped needle was used for the powder injection. A customized dispersion device was designed to direct the injection to the specific Transwell®, eliminating the possibility of cross-contamination and improving the uniformity of powder distribution within the Transwell®. This design had the advantage of applying the powder evenly onto the alginate scaffolding such that the majority of the cultured spheroids were successfully coated for proper application. As shown in Fig. 1, the dispersion device was a horn-shaped hood attached to the blunt tipped needle and placed over the Transwell®. To further improve the uniformity of powder distribution, an internal cone-shaped disperser was suspended inside and near the top of the horn with four supports; all components were 3D printed as one unit. The disperser was intended to induce turbulent flows when the powder was ejected from the syringe. A tube was assembled on top of the horn to insure a constant distance

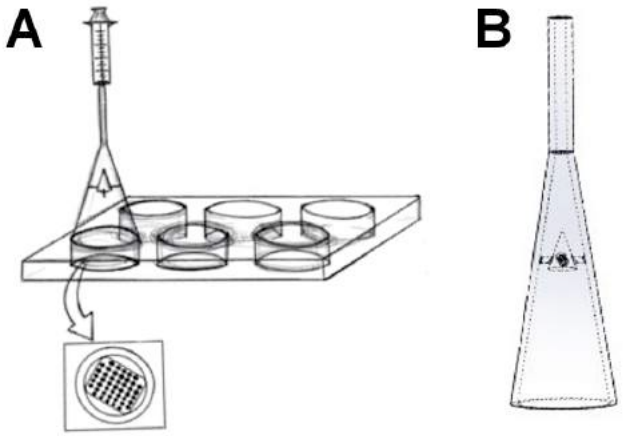

Fig. 1. (A) Schematic showing a customized insufflator placed over a Transwell® for injecting the chemotherapeutic drug powders. (B) The horn attached to the syringe containing an internal cone-shaped disperser to improve uniformity of the powder distribution.

from the tip of the needle to the horn each time the device was used. A comparison was made with and without the disperser in order to demonstrate the effectiveness of the disperser. A color powder with equal size to the drug powder was used in the injection test. To test the powder distribution, a bolus of 3.0 mg of dyed (red) mannitol powder was dispersed through a 3 mL medical syringe and blunt needle. The first test was done without the disperser and the syringe was held approximately two inches above the Transwell® while dispersing the powder through the syringe. The second test utilized the dispersal device; the syringe was inserted into the cylindrical top of the device, the powder was pushed through, and after allowing a few seconds for the powder to settle, the device was removed from the well plate.

III. Results

Initial results from the molds showed a problem with the limited resolution of the 3D printer that resulted in scaffolding with rough surfaces. When seeding the cells, the cells collected around the edges of the recesses and did not form intact, usable spheroids. Acetone, a powerful solvent, effectively dissolved the superficial layers of the plastic as well as in the individual recesses of the mold to create a smoother silicone mold, resulting in large spheroid growth. The initial design for the powder dispersion system was a hollow horn attached to a 3D-printed well plate lid. Although results showed a more uniform spray in comparison to use of solely the syringe and blunt tipped needle device, a higher concentration of powder was still present in the location where the syringe was held. To solve this problem, the final design with the internal cone-shaped disperser eliminated the concentrated spots significantly and aided in a more even dispersal of the powder throughout the entire Transwell®. Pictures of the red powder distributions in the Transwell® showed a clustering pattern without the dispersion device and a uniform pattern with the dispersion as seen in Fig. 2.

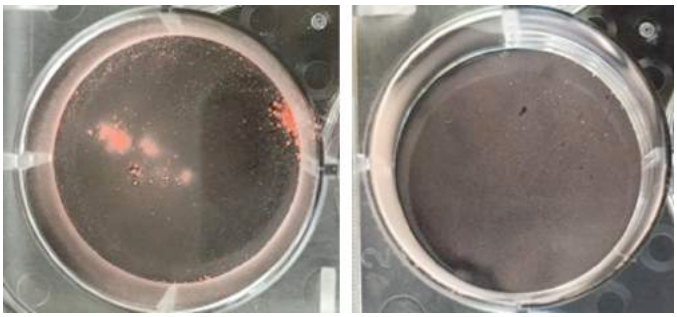

Fig. 2. A model red powder injected into a Transwell® resulted in a clustering pattern without using the dispersion device (left) and a uniform pattern with the dispersion device (right).

IV. Discussion

Suitable mold geometry was determined so that full spheroid formation was achieved. Incomplete spheroids resemble a ring and the cells fail to grow further. The array provides spacing that is desirable for efficient growth and the size produces an efficient amount of spheroids with one use. Use of a six well plate improves the current process and offers another result to compare with the spheroid growths using a 12-well plate for research purposes. The spheroids are a reliable representation of tissue cells present in the lung and are a useful means of studying cells noninvasively.

Results show that an aerosolized powder drug can be evenly distributed with use of this design. Compared to previous methods, cross contamination is now prevented and consistent dispersal is possible, which is important for accurate test results. Because the current high-throughput analysis software method for tracking spheroid growth lacks the capability to measure growth of cells inside the spheroid, it is important that the drug coats the maximum surface area. Future developments include technology to image the inner cells and to track their growth in order to determine drug efficiency with respect to penetration depth.

Acknowledgement

The authors would like to express their gratitude to the University of Rhode Island Undergraduate Research Initiative Awards Program for recognizing and funding this project. The authors would also like to acknowledge Dr. Sweta Gupta and Elisa Torrico (Ph.D. student) of the Chemical Engineering Department at the University of Rhode Island for assisting with research and laboratory procedures.

References

[1] Achilli, T., S. McCalla, J. Meyer, A. Tripathi, and J. Morgan, “Multilayer spheroids to quantify drug uptake and diffusion in 3D,” Molecular Pharmaceutics 11 (7): 2071–2081, 2014.

[2] Lan, H. “Soft UV nanoimprint lithography and its applications,” InTech, Ch. 7, DOI: 10.5772/56186, 2013.

[3] Gong, X., et al., “Generation of multicellular tumor spheroids with microwell-based agarose scaffolds for drug testing,” Plos One, DOI: 10.1371, 2015.

[4] Svoronos, A., N. Tejavibulya, J. Schell, V. Shenoy, and J. Morgan, “Micro-mold design controls the 3D morphological evolution of self-assembling multicellular microtissues,” Tissue Eng Part A. (7-8): 1134-44, 2014.

Graphical User Interface to Generate Waveforms for a Wrist Pulse Simulator Used in Traditional Chinese Medicine Education

Joseph Maestri, Sarah Borges, George Halkidis, Mona Boudreaux,* G. Faye Boudreaux-Bartels, and Ying Sun
Department of Electrical, Computer, and Biomedical Engineering, University of Rhode Island, Kingston, RI 02881, USA;
* A Circle in Time, Wonder Lake, IL 60097, USA. Correspondence email: yingsun@uri.edu

***Abstract*—Pulse diagnosis in traditional Chinese medicine (TCM) involves palpating the radial arterial pulses with three fingers and using the determined pulse characteristics such as strength, depth, and rate to ascertain particular ailments of the patients. TCM specialists are able to detect approximately 28 pulse patterns. Previously, a wrist pulse simulator was developed to generate the palpating forces directly with solenoids, but showed a limited flexibility in specifying the pulse waveforms. This study aimed to improve the previous system by modifying the software, redesigning certain components with 3D printing, and creating a graphical user interface that allows for generation of any desired pulse waveform. By linking hand-drawn waveforms to palpation feelings, the device has provided an innovative pedagogical tool for teaching the practice of pulse diagnosis.**

Keywords—pulse diagnosis; simulator; graphical user interface; traditional Chinese medicine

I. Introduction

Traditional Chinese Medicine (TCM) uses the pulse diagnostic technique as an essential tool for diagnosing certain patient illnesses and diseases [1]. With three fingers (index, middle, and ring fingers) the practitioner palpates the radial pulse at the wrist [2]. The characteristics of the pulse are tested and noted at three different finger depression pressures: "superficial" pressure, "intermediate" pressure, and "deep" pressure [3]. This information enables practitioners to determine the causes of a variety of patient's symptoms.

Previously, a pulse diagnosis simulator was developed based on three solenoids under the control of an embedded microprocessor [4]. In the present study, the original design was further improved and extended in its functionality. The main focus of this project was on the development of a graphical user interface (GUI) such that pulse waveforms can be easily specified and downloaded to the embedded processor for execution. The core of the GUI was an image analysis software capable of tracing a curve in an image and converting it to a time sequence of digital data points. The pulse waveforms could be physiological pressures recorded digitally or on a strip chart. Moreover, because the pulse palpation feelings are often a more abstract concept difficult to describe verbally, the GUI was designed such that hand-drawn waveforms can easily be traced and turned into pulse pressure waveforms delivered via the pulsations of the three solenoids.

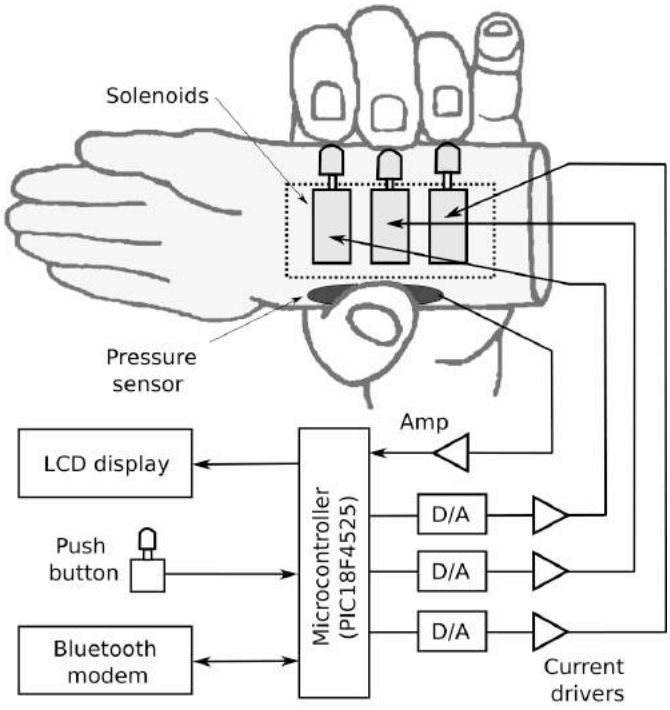

Fig. 1: Schematic diagram of the pulse simulator that uses three solenoids to produce the wrist pulse pressure waveforms.

II. Methods

A. System hardware

As shown in Fig. 1, three solenoids were fitted into a plastic container created by using SolidWorks (Waltham, MA) and 3D printing. The container was placed inside a customized hand model made of silicone rubber. The solenoids moved the plastic pushers that were the contact points for the user's three fingers. The pulsations of the solenoids (SMT-1632S12A-R, Jameco Reliapro) were controlled by the microcontroller (PIC18F4525, Microchip, Chandler, AZ) via three 12-bit serial digital-to-analog converters (TLC5616, Texas Instruments, Dallas, TX) using Darlington-pair transistors as current drivers. A pressure sensor (A401-25, Tekscan, South Boston, MA) was used to record the magnitude of applied pressure via the thumb and, based on the magnitude and the corresponding pulse pressure

setting, adjusted the pulsations of the solenoids accordingly. The firmware for the microcontroller was developed in the C language using the MPLAB integrated development environment (Microchip, Chandler, AZ).

B. *Software development*

Software development for the graphical user interface (GUI) was accomplished in the C++ language using the cross-platform wxWidgets tool (www.wxwidgets.org). The GUI allowed a hand-drawn pressure waveform to be digitized and downloaded to the pulse simulator for execution. The waveform could be either created with a graphic software or drawn on paper and then scanned to an image. The curve tracing process started with a thinning algorithm based on a 4-neighbor connectivity threshold filter [5]. The 4-neighbor connectivity filter used in this design scanned the image with a 3x3 pixel mask, checking the four edge connected pixels to the center pixel against a threshold. If all four edge connected pixels satisfied the threshold requirement, the center pixel was sampled. A median filter was used as an option to smooth the curve while preserving the edges. Then, the x and y coordinates were extracted sequentially from the curve to form a time sequence representing the pressure waveform. The GUI allowed the user to load an image, select the grayscale threshold for the filter, and specify the desired amplitude and time scale for the resulting waveform. The final output was a series of 8-bit numbers corresponding to the coordinates of each pixel satisfying the user selected threshold requirement, as well as a timer value for the hardware. The amplitude of the waveform was scaled to fit within a user selected range, then shifted to the correct starting amplitude for the hardware. The waveform was integrated into the C code in MPLAB, downloaded to the PIC18F4525 microcontroller, and implemented in a custom wave mode in addition to the other preset waveform modes.

III. Results

The wrist pulse simulator was successfully constructed. The GUI was developed on a PC laptop. A selection of drawn waveforms were used to test the GUI and the pulse simulator. As shown in Fig. 2 (left), three conceptual arterial pressure waveforms for young, older, and hypertension cases were drawn freehand. After the curve tracing process, the digitized waveforms were downloaded to the pulse simulator for execution. The output voltages of the D/A converters that drove the solenoids were able to represent the desired waveforms, as shown in Fig. 2 (right).

IV. Discussion

The main contribution of this study was the development and implementation of a graphical user interface that traces and scales user defined pulse waveforms for the wrist pulse simulator. The wrist pulse diagnosis technique – capable of differentiating 28 pulse patterns – is a powerful and essential diagnostic tool in traditional Chinese medicine. However, teaching students to practice pulse diagnosis could be a challenge because of the lack of an effective demonstration for many less frequently occurring pulse patterns. Thus, the GUI

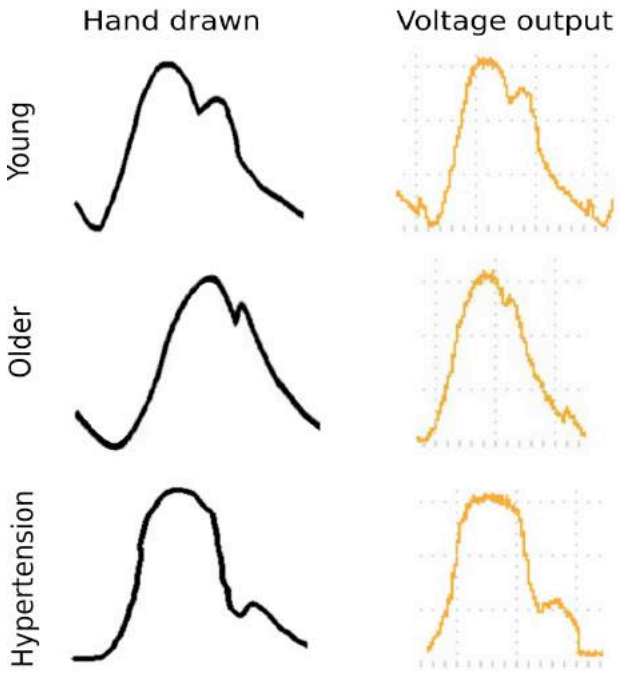

Fig. 2. Hand-drawn wrist pulse waveforms (left) and the corresponding simulator waveforms outputted by the digital-to-analog converters (right).

of the pulse simulator provides a unique possibility to create a certain palpation feeling by designing, drawing, and executing a conceptual wrist pulse pattern. For future work, the GUI will be further improved to allow for the specification of a set of waveforms that represent the time delays among the solenoids and the changes in response to the three different finger depression pressures (superficial, intermediate, and deep). In addition, the GUI will be ported to a handheld device such as a smartphone and the downloading of the waveforms will be made possible via a Bluetooth wireless link.

Acknowledgment

We would like to thank the URI Undergraduate Research Initiative Awards program for their generous financial support of this project. We would also like to thank Dr. Eugene Chabot, James Moretti, and the URI Image Processing Laboratory for their technical support and advice.

References

[1] Walsh, S., and E. King. Pulse Diagnosis: A Clinical Guide. 1st edition. Churchill Livingstone, ISBN-10: 0443102481, 2007.

[2] B. Flaws. The Secret of Chinese Pulse Diagnosis. 3rd edition. Blue Poppy Press, ISBN-10: 1891845586, 2012.

[3] S. Dharmananda, “The significance of traditional pulse diagnosis in modern practice of Chinese medicine,” http://www.itmonline.org/arts/pulse.htm, August, 2000.

[4] S. McLellan *et al*., "A microprocessor-based wrist pulse simulator for pulse diagnosis in traditional Chinese medicine," 40th Annual Northeast Bioengineering Conference, April 25-27, 2014.

[5] Sonka, M., V. Hlavac, and R. Boyle. *Image Processing, Analysis, and Machine Vision*, 4th ed., CL Engineerin, ISBN-10: 1133593607, 2014.

Balance Board with Embedded Sensors for the Rehabilitation of Ankle Injuries

Brett Kotowski[1], Matthew Barbin[1], Corey Gomes[1], Craig Simpson[2], Eugene Chabot[1]
[1]Department of Electrical, Computer and Biomedical Engineering,
University of Rhode Island, 45 Upper College Road, Kingston, RI 02881
[2]Comprehensive Physical Therapy, North Smithfield, RI 02896

Abstract— **The purpose of this project is to create a balance board device that can quantitatively assess a patient's progress during ankle rehabilitation. Real-time ankle attitudes are collected from this device for real-time and post treatment assessment of ankle proprioception. With the use of an Arduino Nano, a 9-axis Magnetic Angular Rate Gravity (MARG) sensor embedded into a balance board, and a PC application, data are collected and statistically analyzed to monitor the static and dynamic characteristics of the ankle motion.**

I. Introduction

Ankle injuries are one of the more common injuries of the lower extremities. An estimated 25,000 Americans suffer from an ankle injury each day. Ankle sprains account for almost half of sports injuries [1]. Following an injury to the ankle, physical therapy is often prescribed to rehabilitate weak muscles, regain range of motion, and restore normal function. In addition to strengthening and range of motion exercises, one of the major components of ankle rehabilitation is proprioceptive training. Proprioceptive training involves the retraining of ankle neuroreceptors that provide position sense feedback to the brain. These specialized neuroreceptors are embedded in the ligaments and tendons that control movement of the ankle. Nerve signals are sent from these neuroreceptors (sensory) to the brain, which sends signals via the efferent (motor) nerve pathway, back to the muscles of the ankle to control ankle movements. This proprioceptive system plays a large role in balance and coordination when walking on uneven surfaces, running, jumping, and performing agility activities.

Previous investigators have used various methods to quantify and measure ankle proprioception. Amy S. N. Fu et al [2], in a study measuring ankle proprioception in basketball players, used the Passive Ankle Joint Report (PAJR) test, where the ankle is placed in various positions of ankle plantar flexion and the patient is asked to identify the position with accuracy. This method uses positions in the plantar flexion and dorsiflexion plane and does not account for positions in the inversion and eversion plane of ankle motions. As the vast majority of ankle sprains occur in the inversion and eversion planes, this is important motion to consider. More recent studies (Miralus et al [3]) have utilized complex 3D motion analysis systems incorporating multiple cameras and position sensors placed on the body. These systems are very expensive and require elaborate set up procedures which are not practical in the average rehabilitation setting. A wobble board design demonstrated a lower cost and simplified setup, but was biased in the pitch estimate by the motion of the user [4].

The device proposed in this paper enhances the measurement capability of an accelerometer based wobble board design by capturing rotational components including yaw (around the axis perpendicular to wobble board surface) with a gyroscope and magnetometer. These additional sensors help reduce the dynamic error of the roll and pitch estimates as well as providing an estimate of heading.

II. Methods

The materials used for this project include the Arduino Nano, a Magnetic Angular Rate Gravity (MARG) sensor, and a PC application. The Arduino Nano is responsible for interfacing the MARG sensor, both configuration and data handling, and providing data to the PC application over a USB connection (see Fig. 1.). A 9-axis MARG (MPU9250, Invensense, Inc.) is utilized with a triple axis accelerometer, magnetometer, and gyroscope integrated. Both the microcontroller and MARG sensor were integrated into the center of the wobble board platform. While not crucial to the design, the MARG sensor is placed close to the center of the platform. An area of approximately 2 square inches is required for the electronics. A USB cable connects this embedded hardware to a PC to provide power and data extraction facilities.

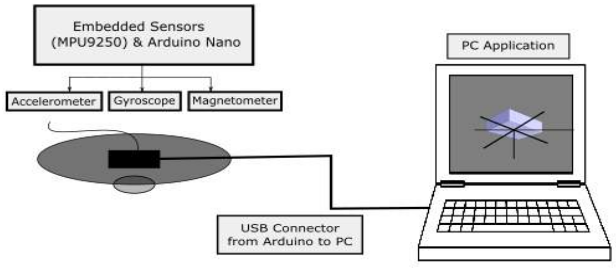

Fig.1. Block diagram of the balance board embedded with sensor hardware and connected to a PC for real-time feedback and analysis.

A PC application based on Qt software libraries was constructed to calculate the wobble board orientation (roll,

pitch, and yaw), show a real-time 3D representation, and provide data recording facilities. The wobble board pose is estimated by utilizing a computationally efficient gradient descent based orientation filter developed by Madgwick [5]. The quaternion based Attitude and Heading Reference System (AHRS) has been configured to operate at 200 Hz sample rate for accelerometer and gyroscope data with a 100 Hz sample rate of the magnetometer. The AHRS algorithm fuses sensor data to estimate the orientation at a rate of 200 Hz. With an estimated pose, the results are presented with an OpenGL rendered model of the wobble board. The display has been designed to provide visual feedback for the patient to train for compliance with instruction given by the physical therapist. After a training period, the physical therapist has the ability to record test data for proprioceptive assessment. The data is stored in a comma delimited text format (CSV) for import into data analysis software packages.

In order to assess the accuracy of the device, a test setup was constructed. A factory calibrated MARG sensor is utilized without field calibration for temperature drift or hand and soft iron biases on the magnetometer. Two wooden blocks, one orientated at 45 degrees and the other at 14 degrees, provided fixed poses for the electronics. Per the axis conventions of the MPU9250, the circuit board was placed on the table (0 degrees) and then placed on a block causing a rotation in a specified axis. Each measurement consisted of repeating the process of placing at a 0 degree orientation, placing at a rotated pose, and then back to the 0 degree reference position waiting greater than 5 seconds between positions. The measurement process was repeated 8 times to collect statistics (mean and standard deviation) of the position for positive and negative rotations in each of the X, Y, and Z axes. The device's PC application recorded the test results. At the conclusion of all of the data collection, the 8 measurements from each pose were extracted by selecting a value from the stationary period at each rotation.

III. Results

As was described in the prior section, block tests were conducted. The statistics from the tests are reported in Table 1. The negative and positive rotations correspond to the conventions designated by the MPU9250.

TABLE 1. MEAN (μ) AND STANDARD DEVIATION (σ) OF 14 AND 45 DEGREE ROTATIONS

Direction (deg)	Negative rotation		Positive rotation	
	μ	σ	μ	σ
45 (X-axis)	45.102	0.516	46.732	0.223
45 (Y-axis)	43.899	0.542	43.989	2.012
45 (Z-axis)	39.727	1.372	39.008	2.739
14 (X-axis)	13.354	0.202	13.141	0.307
14 (Y-axis)	13.693	0.216	12.525	0.217
14 (Z-axis)	11.055	0.801	10.646	0.495

IV. Discussion

A wobble board based measurement platform has been presented for use during ankle rehabilitation. The design has adapted techniques often employed in aircraft navigation to add improved estimates of the wobble board pose. The wobble board provides an inexpensive platform for both in office and at home rehabilitation. The addition of a gyroscope to an accelerometer based design reduces some of the artifacts related to the board hitting the ground (large magnitudes in acceleration) and biases added to the gravity vector during motion. Also, a magnetometer allows for an estimate of the rotation around the gravity vector, which is lacking in prior wobble board work [4].

The presented work was able to establish real-time communication with a computer and track, in real time, the dynamic movements provided by the patient's foot and ankle. While representing an un-calibrated sensor, static rotational results are reported in Table 1. The device reflects a repeatable measurement with a low standard deviation (less than 3 degrees). Calibration of the device for temperature and hard/soft iron biases can be expected to improve the absolute accuracy, but it is less likely to reduce the variance. The direction of the largest error is the Z axis, which corresponds to the rotation around the gravity vector. This can be likely attributed to biases introduced by hard and soft iron biases.

Future work includes improving the accessibility of the device and further assessments on performance. To improve upon the ease of use in a clinical setting, the addition of a Bluetooth interface for communication to a handheld device is anticipated. Further studies are planned to quantify the accuracy of the positional readings during motion and after the cessation of motion. This low-cost measurement device with a further quantification on performance could assist physical therapists in analyzing proprioception, determining the most effective therapy to regain or enhance proprioception, and reducing the risk of injury to the ankle in the future.

Acknowledgement

Thanks are paid to the Undergraduate Research Initiative for the funding of this project.

References

[1] V. Ibrahim, Z. Meyler, and A. Panagos, "Ankle Sprains and the Athlete", American College of Sports Medicine, 2012.

[2] A. S. Fu and C. W. Hui-Chan, "Ankle joint proprioception and postural control in basketball players with bilateral ankle sprains," Am. J. Sports Med., vol. 33, no. 8, pp. 1174–1182, 2005.

[3] M. Iris, S. Monterde, M. Salvador, I. Salvat, J. Fernandez-Ballart, and B. Judith, "Ankle taping can improve proprioception in healthy volunteers," Foot Ankle Int., vol. 31, no. 12, pp. 1099–1106, 2010.

[4] S. Volpe, D. Demers, E. Simpanen, E. Chabot, and C. Simpson, "Balance board rehabilitation device for ankle proprioception assessment," in Biomedical Engineering Conference (NEBEC), 2015 41st Annual Northeast, 2015, pp. 1–2.

[5] S. O. H. Madgwick, A. J. L. Harrison, and R. Vaidyanathan, "Estimation of IMU and MARG orientation using a gradient descent algorithm," in 2011 IEEE International Conference on Rehabilitation Robotics (ICORR), 2011, pp. 1–7.

Android Based Device for Emergency Responders to Indicate Distress in Extreme Environments

M. D. Twardowski, J. M. Pfisterer, T. A. Barnes, R. M. Blease, E. Chabot, Y. Sun
University of Rhode Island
45 Upper College Rd, Kingston, RI 02881

***Abstract*—An Android based Personal Alert Safety System (PASS) combined with heart rate (HR), respiration rate (RR) and interior face shield temperature monitoring can provide a powerful, low cost platform for first responders to indicate stress in extreme environments. Combining an Arduino sensor array with Bluetooth communication allows the Android phone to record movement and physiological data that can be used to trigger various alarms automatically. The HR algorithm results were verified through comparison to a commercially available pulse oximeter system. It was found to have an accuracy within +/- 2 beats per minute. This system is designed to be retrofitted into pre-existing safety equipment, eliminating the need for overall equipment redesign or purchase of new, costly equipment. The ease of deployment and overall effectiveness of this design has the potential to be a critical piece of lifesaving equipment for first responders worldwide.**

I. Introduction

Firefighters routinely enter hazardous environments in performance of their duties. A Personal Alert Safety System (PASS) is a small battery powered safety device worn by each firefighter that sounds a loud audible alert to notify others in the area when that firefighter is in distress. These devices automatically trigger the alarm if motion is not sensed within a short period of time, typically no longer than 30 seconds. Ten seconds before an alarm, a low intensity tone sequence warns a firefighter that an alarm will to occur if motion is not detected [1].

Additional physiological monitoring has been proposed to provide other indicators of distress. In particular, cardiovascular events account for 45% of deaths among firefighters on duty. In contrast, these events account for 15% of all deaths that occur on the job. Fire suppression, which represents only 1 to 5% of firefighters' professional time each year accounted for 32% of the deaths caused by cardiovascular events. Other non-fire emergency responses do not have a significant increase in risk of death from cardiovascular events [2]. Duckworth et al. required the firefighter to don a shirt [3] or wear a strap on the forehead that contains the physiological sensors [4].

A design is presented herein that utilizes a commonly available platform, namely Android based hardware, that can be paired with Bluetooth connected sensors (refer to Fig. 1.). The sensor array design is integrated in the Self Contained Breathing Apparatus' (SCBA) mask to provide basic physiological monitoring without the need for firefighters to don additional gear or increase their preparation time.

II. METHODS

A. Hardware

A Bluetooth equipped Arduino board (RedBearLab BLE Nano), a combined temperature-barometric sensor (BMP180), and a photoplethysmogram sensor (PPG) [5] were affixed to a Scott air mask such that the PPG would come into contact with the lateral cartilage of the nose. The combined temperature-barometric sensor is placed within the mouthpiece to measure the airflow coming from the SCBA without impeding it and to monitor the internal mask temperature to generate an alarm if the integrity of the polycarbonate face shield had been compromised. The entire assembly is powered by a polymer battery.

B. Arduino Software

The heart rate (HR), respiration rate (RR), and temperature measurements are all performed on the Arduino. The PPG voltage waveform is band pass filtered (0.8 to 5.0 Hz) and the HR is calculated by using a moving window method that is 3/5's the width of the previous pulse in the resulting waveform [4]. If the PPG sensor loses contact with the skin, the measured voltage is zeroed, and the HR calculation and the corresponding alarm is disabled. This feature can reduce standby power consumption and prevents false HR alarms [5].

The pressure waveform from the barometer is filtered using a nine-point median filter to smooth motion and speech artifacts. The RR is then calculated by using a moving window method similar to the HR algorithm. A BLE GATT protocol transmits the HR, RR, and mask temperature to an Android phone.

C. Android Software

The Android operating system was chosen due to the affordability and general availability of the hardware. The

This study was supported by a grant from the 2015-2016 Undergraduate Research Initiative Awards of the University of Rhode Island.

PASS app, called Biomedical Personal Alert Safety System (bPASS), requires a minimum Android SDK of 4.0 for installation on a phone. The app displays current alarm status, and will display HR, RR and mask temperature if an alarm has been triggered. The app also allows for a user to trigger the alarm manually, and disable any active alarm.

The bPASS app uses the accelerometer of the phone to detect motion. The motion detection algorithm calculates the linear acceleration for each axis [6]. If the linear acceleration for any axis is above a predetermined threshold, the algorithm flags that motion has occurred.

A timer object is used to track the elapsed time since motion has occurred. When the timer reaches 20 seconds, a pre-alarm is triggered and is played through the phone's speaker. When the timer reaches 30 seconds, the full PASS alarm is triggered and played at full volume. At any time prior to 30 seconds, detected motion will reset the timer to zero. Once the full PASS alarm is activated, it can only be disable by a user double tapping a button in the app. This action will also reset the timer to 0 and monitoring will be continued until disabled.

A HR alarm will be triggered when a wearer's heart rate exceeds 99% of their maximum HR for a period of time. The wearer's maximum heart rate is determined by subtracting their age from 220 [7].

Fig. 1. bPASS Data Flow – physiological data is relayed to the Android phone. Any triggered alarms would be heard audibly and relayed to a local base station.

III. DISCUSSION

With the development of this prototype, a tool has been presented which will enhance the overall safety of firefighters and Emergency Medical Services (EMS) at an incident by keeping everyone apprised of their status. The design described has been constructed with HR, RR, and temperature sensor data transmitted to the Android device with the motion alarm and physiological alarms functioning as intended. An example of the acquired pressure sensor data is shown in Fig. 2. A qualitative analysis of the HR algorithm has shown performance within +/- 2 beats per minute when compared to a CMS50E Pulse Oximeter. In the current model, alarms are played audibly through the speaker on the phone. An external speaker is planned which will be able to play the alarm at the 95 dB regulation [1].

The bPASS system is designed with close attention to user friendliness, ease of incorporation into preexisting equipment, and national safety standards. It potentially can provide a vast improvement upon the current PASS system. As acceptance of this and similar technology may be stifled by liability and privacy concerns, the user's privacy is maintained by limiting the physiological data to the phone and only broadcasting an alarm condition.

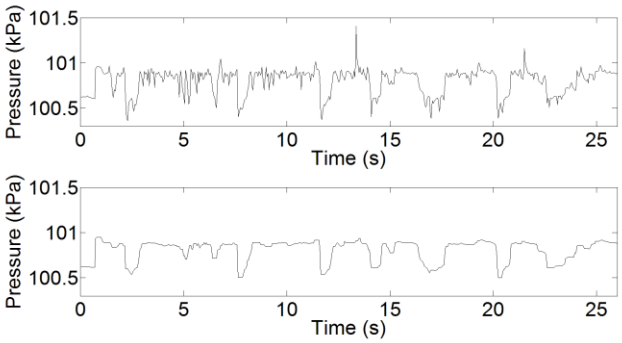

Fig. 2. Unfiltered Pressure Waveform (a), Median Filtered Pressure Waveform (b)

EMS responding to mass casualty and active shooter events could benefit from bPASS. Due to the unknown nature of when these events may occur, current PASS devices are not a feasible option. The bPASS app would only monitor their movement when remotely activated by being in proximity to a current incident response. This could give EMS and law enforcement better command and control within incident areas.

While the design accomplishes the goals set forth to demonstrate feasibility, future work could be pursued to further enhance the design. Putorti et al. [8] observed little difference in the peak inside air temperature of the SCBA mask, and significant increases in the interior surface temperature of the face shield at different heat fluxes. Adding a temperature sensor located on the face shield interior might help monitor face shield integrity. In addition, PPG measurements are susceptible to motion artifacts, but Elgendi et al. [9] have suggested a method that uses two event related moving averages to automatically determine wearer specific thresholds to increase HR estimation accuracy.

REFERENCES

[1] *Standard on Personal Alert Safety Systems (PASS)*, National Fire Protection Association, 1982

[2] N. Kales, et. al. "Emergency Duties and Deaths from Heart Disease among Firefighters in United States," *N Engl J Med*. vol. 365, pp. 1207-1215. Mar. 2007.

[3] J. Duckworth, "WPI Precision Personnel Locator System - Evaluation by First Responders," *ION-GNSS Session D3: Indoor Positioning*. Sept. 2007.

[4] W. S. Johnson, "Development of a Singal Processing Library for Extraction of SpO2, HR, HRV, and RR from photoplethysmographic Waveforms," M.S. thesis, Worchester Polytechnic Institute, Worcester, MA, 2006.

[5] J. Murphy, and Y. Gitman, "Open hardware," 2016 [Online]. Available: http://pulsesensor.com/pages/open-hardware.

[6] Developer.android.com, "Motion Sensors | Android Developers," 2016. [Online]. Available:http://developer.android.com/guide/topics/sensors/sensors_motion.html.

[7] H. Tanaka, K. D. Monahan, D. R. Seals, "Age related maximum heart rate revisited," *J Am Coll Cardiol*. vol. 37(1) pp. 153-156. Jan. 2001.

[8] A. Putorti, et. al., "Thermal Performance of Self-Contained Breathing Apparatus Facepiece Lenses Exposed to Radiant Heat Flux," National Institute of Standards and Technology, Gaithersburg, MD, NIST Technical Note 1785, Feb 2013.

[9] M. Elgendiet, et. al. "Systolic Peak Detection in Acceleration Photoplethysmograms Measured from Emergency Responders in Tropical Conditions," *PLOS One*. vol. 8, pp. 1-11. Oct 2013.

Heart Rate Age: Baroreflex Sensitivity in Response to Valsalva Maneuver and Sudden Standing-Up

Amanda Junkins, Callie Thomas, Eugene Chabot, Ph.D., Ying Sun, Ph.D.
Department of Electrical, Computer and Biomedical Engineering, University of Rhode Island, 4 East Alumni Avenue, Kingston, RI 02881, USA. Correspondence email: yingsun@uri.edu

***Abstract*—The baroreflex sensitivity decreases with age. In this study, the *Heart Rate Age* (HRAge) is proposed as an index to reflect the viability of the autonomic function. A portable device was developed to assess the induced heart rate variability (HRV) in response to an intervention of either the Valsalva maneuver or the sudden standing-up movement. A real-time QRS detection algorithm was implemented during a 15-s rest period with the subject in a seated position followed by a 15-s intervention. The induced HRV was used to estimate the age based on data extrapolated from literature. A prospective IRB-approved human study has been conducted to collect data for improving the HRAge estimation using additional parameters such as sex and body mass index (BMI).**

Keywords—heart rate age; baroreflex sensitivity; Valsalva maneuver; sudden standing-up; autonomic function; biomedical instrumentation; electrocardiogram; embedded system design

I. Introduction

Heart rate variability (HRV) is defined as the variation in the beat-to-beat heart rate. Monitoring HRV can lead to early detection of eventual heart problems or arrhythmias. For example, individuals with a lower HRV than normal ranges have been shown at an increased risk of developing coronary heart disease [1]. It has been determined that, in general, the HRV of an individual decreases as age increases. Thus there is a correlational relationship between HRV and age-related autoregulation [2].

The problem being addressed in this study was the lack of a quick method for assessing the HRV as well as a meaningful index to reflect the viability of the autonomic function. A novel index, the Heart Rate Age (HRAge), is proposed to assess a person's physiological age in terms of the induced HRV. The Valsalva maneuver—attempted forceful exhalation against a closed airway—suppresses the venous return to the heart, thereby inducing baroreflex to increase the heart rate. The sudden standing-up movement momentarily lowers the carotid artery pressure and can also induce baroreflex to increase the heart rate. In this project, a portable embedded instrument was developed that measures a single-channel electrocardiogram (ECG) and determines the HRV induced by an intervention such as the Valsalva maneuver and the sudden standing-up from a seated position.

II. Methods

A. Instrumentation for Assessing the Induced HRV

As shown in Fig. 1, an embedded system based on a PIC18F4525 microcontroller (Microchip, Chandler, AZ) was developed to implement an experimental protocol that assessed the induced HRV from a single-channel recording of the ECG signal. The experimental protocol consisted of a 15-s ECG recording with the subject in a seated position, followed by another 15-s ECG recording with a test condition of either the Valsalva maneuver or the sudden standing-up. Real-time QRS detection was accomplished by the multiplication of backward differences (MOBD) algorithm [3]. The beat-to-beat heart rates were recorded and used to determine the normal heart rate (HRn) and the tested heart rate (HRt). The induced HRV was given by: HRV (%) = (HRt – HRn) / HRn x 100%.

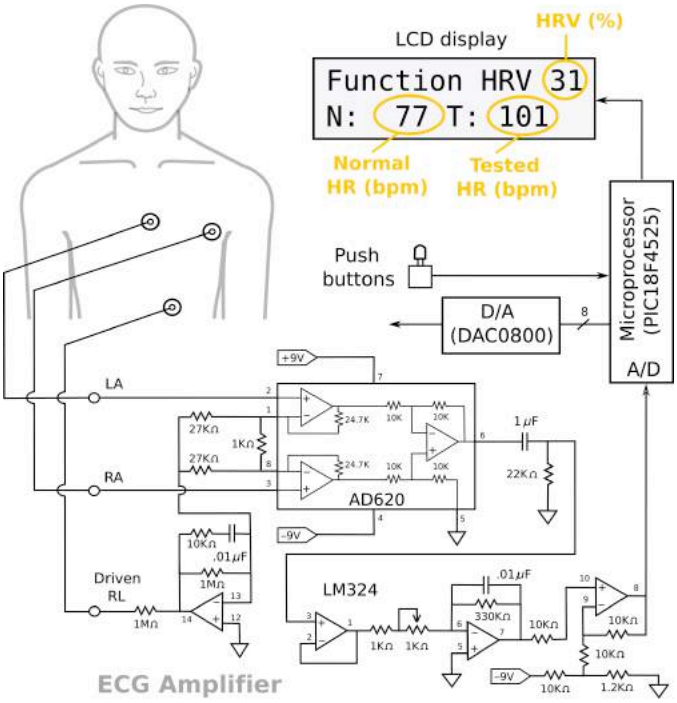

Fig. 1. Schematic diagram of the embedded instrument for measuring a single-channel ECG and executing a protocol to assess the induced HRV.

B. HRAge Analysis

In order to use the induced HRV for the HRAge estimation, a literature search was conducted. While no specific clinical data pertaining to the experimental protocol in this study were found, useful relationships were extrapolated from data reported by O'Brien et al. [2]. Assuming an average heart rate of 75 bpm for all age groups, the data from [2] resulted in the curves as shown in Fig. 2. Linear regression analyses resulted in the following relations:

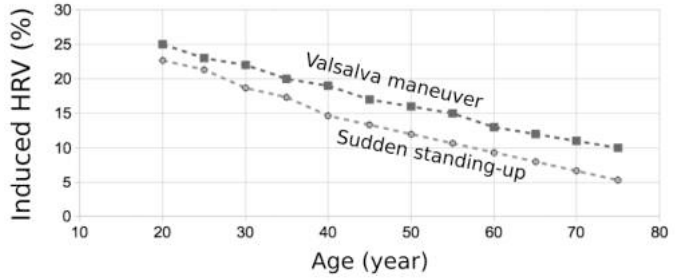

Fig. 2. HRV vs. age relationships for Valsalva maneuver and standing extrapolated from data reported by O'Brien et al. [2] by assuming a normal resting heart rate of 75 bpm for all age groups.

$$\text{HRV (Valsalva)} = -0.365\ \text{Age} + 40\ (\%);\quad r = -0.996 \quad (1)$$

$$\text{HRV (Standing)} = -0.315\ \text{Age} + 28\ (\%);\quad r = -0.994 \quad (2)$$

The above relations could be used to estimate HRAge :

$$\text{HRAge (Valsalva)} = 274\ (40\% - \text{HRV}) \quad (3)$$

$$\text{HRAge (Standing)} = 317\ (28\% - \text{HRV}) \quad (4)$$

C. IRB Approved Prospective Study

A prospective human study was approved by the local IRB to obtain more accurate relations for the HRAge estimation. The study protocol includes an anonymous group of (40) volunteers of widely dispersed ages. In addition to the HRV tests with the Valsalva maneuver and the sudden standing-up, the subjects' age, sex, and body mass index (BMI) are collected.

III. Results

As shown in Fig. 3, the embedded instrument was developed on a breadboard with a customized printed circuit board for ECG recording. The system firmware was developed in the C language using the MPLab integrated development environment and a ICD3 in-circuit programmer (Microchip, Chandler, AZ). Two push buttons were used to allow for changing the operational modes. A digital-to-analog convert (D/A) was also implemented to output internal data for debugging purposes. Although implemented on a breadboard, the device was portable and robust enough to support the IRB approved human study. The human study is currently on-going. Table I shows the preliminary results from 3 subjects.

IV. Discussion

In this study, a method and a device were developed for estimating the heart rate age (HRAge) as an index for the baroreflex sensitivity. The induced heart rate variability (HRV) can be quickly assessed with a 30s procedure that measures the normal resting heart rate and the tested heart rate under an intervention such as the Valsalva maneuver and the sudden standing-up movement. The formulas for estimating the HRAge were initially extrapolated from data in literature and will be further improved with a prospective study and by using additional parameters such as sex and BMI. The initial results in Table I showed a significant overestimation of the HRAge for the two young women subjects, which is consistent with the findings in previous studies that women have lower HRV than men [4]. Future work includes the completion of the prospective human study, porting the instrumentation to a handheld device such as a smartphone, and transferring the research to a commercial product.

TABLE I. Preliminary results for HRAge estimation

Subject ID	Sex	Age	HRV (Valsalva)	HRV (Standing)	HRAge (Valsalva)	HRAge (Standing)
1	F	25	20%	12%	55	51
2	F	25	16%	7%	66	67
3	M	50	18%	11%	60	54

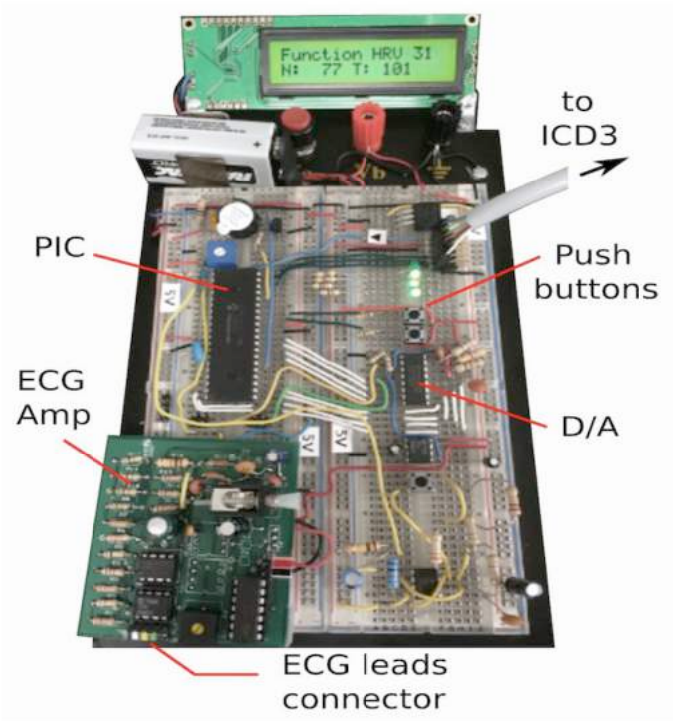

Fig. 3. Prototype system for the measurement of induced HRV.

Acknowledgment

The authors would like to express their gratitude to the University of Rhode Island Undergraduate Research Initiative Awards Program for recognizing and funding this project.

References

[1] Ramaekers, D., H. Ector, A. E. Aubert, A. Rubens, and F. Van De Werf. "Heart Rate Variability and Heart Rate in Healthy Volunteers." *European Heart J, vol.* 19, pp. 1334-1341, 1998.

[2] O'Brien, I. A. D., P. O'Hare, and R. J. M. Corrall. "Heart rate variability in healthy subjects: Effect of age and the derivation of normal ranges for tests of autonomic function." *British Heart J, vol.*55, pp. 348-354, 1986.

[3] Sun Y., S. Suppappola, T. A. Wrublewski. Microcontroller-based real-time QRS detection. *Biomed. Instrum. & Technol.*, vol. 26(6), pp. 477-484, 1992.

[4] Huikuri, H. V., et al. "Sex-related differences in autonomic modulation of heart rate in middle-aged subjects." *Circulation,* vol. 94, pp. 122-125, 1996.

Real Time Visual-to-Tactile Substitution Using AIMS on Android

Justin Pelletier, Richard Melpignano, J. Cody Goldberg, Eugene Chabot, PhD, and Ying Sun, PhD
Department of Electrical, Computer and Biomedical Engineering
University of Rhode Island, Kingston, RI 02881-0805 USA

***Abstract*—Using real-time image processing through a custom Android application, this device is able to track motion when a user is stationary and relay this information through Bluetooth to a microprocessor on a belt. This belt contains 15 small vibrating motors that activate in a pattern corresponding to the location, direction, and size of motion acquired from the Android motion tracking system.**

I. Introduction

As derived from the 2014 American Census Survey, an estimated 7.3 million people in the United States are reported to have a visual disability [1]. Some of the most common causes of vision loss include macular degeneration, glaucoma, detached retina, and diabetic retinopathy [2]. All of these visual impairments can lead to difficulty navigating public spaces safely with an increased potential of injury. For severe visual impairments, the white cane and auditory feedback are the primary resources for information on surroundings, which can leave the subject unaware of critical details about approaching objects.

Sensory substitution assistive technology devices have been proposed to augment the individual's environmental awareness. In particular, devices have been constructed to estimate motion in the field of view with auditory feedback [3] and tactile feedback using vibration along the waist for cueing [4]. These prior efforts lack identification of a commonly available, low cost platform.

Extending upon the tactile feedback of motion information [4], an assistive device is presented that pairs Android programming, Bluetooth low energy (BLE), and vibrotactile feedback. The Android platform encapsulates the complexity of the image processing to allow for further enhancements as technology advances while decoupling the specialized hardware through Bluetooth communication. Vibrotactile feedback of motion information attempts to minimize sensory overload and interference with typical environmental feedback mechanisms.

II. Methods

The system, seen in Fig. 1, involves two main components, a belt and a chest plate, that are connected through Bluetooth, relieving the system of extraneous wires. The Android based phone rests on the chest piece, along with the rechargeable battery pack, while the vibrating motor array and all other electronic components are mounted on the belt.

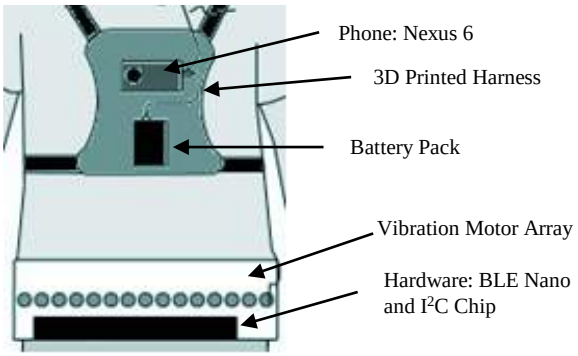

Fig. 1. Visual representation of the system. Electrical components are encased in black below motors on the belt. The external battery pack can be seen below the phone on the chest piece.

A. Chest Plate

The chest plate components are custom designed and 3D printed using Acrylonitrile Butadiene Styrene (ABS) plastic. Included in the design is a retention structure for the Android phone, namely a Motorola Nexus 6, and associated foam padding to dampen vibration and protect from damage. Nylon straps and buckles are integrated into the plate for hands-free use and ease of removal. A connection from the phone to an external battery pack, also securely mounted, is included for long periods of use. All components are designed for removal or replacement by the user.

B. Belt

All other electrical components are mounted upon a polyester belt. A series of 15 pockets are sewn on the inside surface, tight to the users abdomen, holstering one vibrating motor each. All motors are controlled by a BLE-Nano, which receives signals from the Android device wirelessly and modifies motor state through an Inter-Integrated Circuit (I^2C) serial port expander. As illustrated in Fig. 2, each output pin on this port expander drives the gate of a MOSFET transistor setting the state of a motor on the belt. This array of motors runs horizontally along the ventral side of the user's abdomen with a spacing of approximately 3.5 centimeters on center.

C. Android Motion Tracking

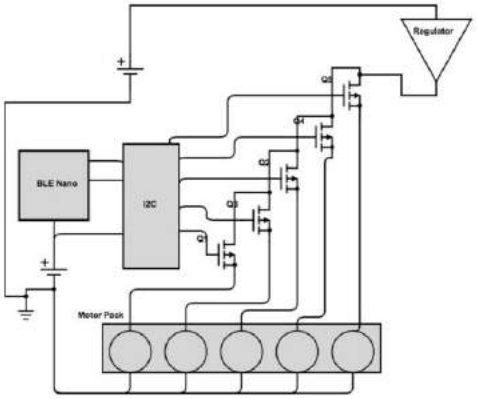

Fig. 2. Block diagram of electrical components hosted on the belt: Black circles represent motors. This diagram only illustrates one section of the belt for simplicity; the process is repeated for each section.

Using a modified form of the AIMS algorithm [5], motion in the frame captured by the camera is estimated utilizing the Android device. Once an image is captured by the camera, three passes are performed on the YUV image provided. The first pass performs the frame subtraction against the background image, which is captured and or updated when the device is stationary as determined by a threshold on accelerometer data of the Android device. A binary image is generated by applying a threshold to the differences of the images. Secondly, a mean 3-by-3 kernel based low pass filter is applied to the binary image. This low pass filter will remove speckle noise that exists in various parts of the image, which is assumed to be unrelated to movement of an object in view. Finally, a third pass entails collapsing the 2D binary image into a vector representative of the belt feedback elements. This collapse of the image is performed on the image's vertical dimension by calculating a sum and applying a threshold. With a one dimensional result, a motor's state is determined by summing and applying a threshold to the proportion of pixels corresponding to the particular motor. During this pass, a bitmap to be displayed on screen is generated from the binary image (see Fig. 3).

III. Discussion

Fig. 3 illustrates an output of the assistive device described. Operation of the system is considered real-time with a frame rate exceeding 30 frames per second. The rate of pattern modification on the belt is commensurate with the frame rate, but perceptual limits need further investigation to assess accuracy of the information perceived, such as object position, size, and direction of motion. Prior work [4], while not directly representative, suggests the accuracy will degrade with objects translating across the field of view, but may be further impacted by the independent nature of each stimulator. The number of patterns that could be presented are increased, which allows for more than one object in the field of view, adding to the cognitive complexity. Future human studies aim

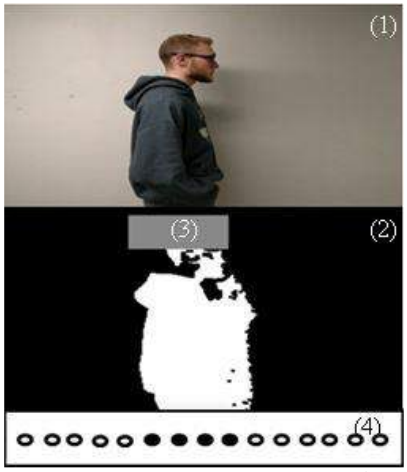

Fig. 3. The top image (1) shows the live camera view of a walking person. A live view of the modified AIMS algorithm capturing the moving person is shown in (2). The gray bar (3) indicates the detected motion and the portion of vibration motors (4) that are correspondingly fired are shown in the bottom.

to assess the user's ability to extract information including the number of objects, and size, location, and direction of the objects. Additionally, mechanisms to improve the operation while the user is non-stationary could be explored including image stabilization.

Acknowledgement

The authors would like to express their gratitude to the University of Rhode Island Undergraduate Research Initiative Awards Program for recognizing and funding this project. The authors would also like to thank Tanya Wang for her assistance throughout the design and implementation processes of this project.

References

[1] United States Census Bureau, "2014 American Community Survey 1-Year Estimates." [Online]. Available: http://factfinder.census.gov/faces/tableservices/jsf/pages/productview.xhtml?pid=ACS_14_1YR_S1810&prodType=table.

[2] W, Erickson, Lee, C., von Schrader, S. (2015). "Disability Statistics from the 2013 American Community Survey (ACS)." Ithaca, NY: Cornell University Employment and Disability Institute (EDI). Retrieved December 1, 2015

[3] B. K Volpe, M. J. Colletti, and J.T. Sudario-Cook, The Android Based Visual Sensory Substitution Device University of Rhode Island, 2015.

[4] E. Chabot Methods and analysis of a wearable, linear, vibrotactile array to relay motion information for visual sensory substitution. University of Rhode Island, ProQuest, UMI Dissertations Publishing, 2011. 3488409.

[5] X. Han, "Active image motion seeking (AIMS) camera system," Ph.D. dissertation, University of Rhode Island, 2002.

An Electronic Model for Vesicle Induced Cell Membrane Capacitance Changes

Lisa Rosenberg, Morgan Hammick, Stephen Sladen, Tanya Wang, Jiang Wu, Ph.D., and Ying Sun, Ph.D.
Department of Electrical, Computer and Biomedical Engineering, University of Rhode Island,
4 East Alumni Avenue, Kingston, RI 02881-0805 USA. Correspondence email: yingsun@uri.edu

***Abstract*—This project aimed to develop an electronic model for simulating the dynamic changes of cell membrane capacitance due to vesicle transportations. Vesicle capacitances on the order of 10 fF were simulated by switching between two carefully calibrated branches of series-connected capacitors. The experimental results obtained with a commercially available high-precision capacitance meter showed that it was possible to measure a capacitance change on the order of 100 fF with a time resolution of about 0.5 s. Although this precision was still insufficient for measuring the vesicle capacitance, the real-time testing platform should be useful for developing more advanced algorithms and instrumentations capable of monitoring the vesicle activities during exocytosis and endocytosis.**

Keywords—capacitance measurement; electronic model; vesicle capacitance; cell membrane capacitance

I. Introduction

Cell membrane capacitance is directly proportional to cell surface area, since membrane composition, thickness, and dielectric constant, are all invariant and not changed by differences in membrane protein density [1],[2]. Thus, it is possible to monitor cellular capacitance fluctuations as a measure of cell surface area changes that occur with exocytosis and endocytosis events when vesicles move through the membrane [3],[4].

In developing a cell membrane capacitance measuring system, it is necessary to have an easy-to-use and low-cost cell membrane model to simulate the static and fluctuating membrane capacitance, for experimenting with live cells is costly, time-consuming, as well as, hard to control. In this project, such a model is to be designed. It is capable of simulating different levels of membrane capacitance changes with programmable patterns as well as static membrane resistance and capacitance.

Cell membrane capacitance is usually in the range of a few pico-Farads (pF), and its change induced by a single vesicle is tens of femto-Farads (fF). This small capacitance change makes it very difficult to implement the model with standard capacitor nominal values. Previously an electronic instrument was developed [5] to model the cell membrane capacitance; however, it did not have the provision for simulating small capacitance changes due to vesicle activities. In this project, a novel approach was proposed, which took advantage of the inherent deviation among standard capacitors to achieve the small capacitance variations.

II. Methods

A. Hardware

Figure 1A shows the schematic of the proposed electronic cell membrane model. Resistor Ra (1MΩ) simulates the access resistance. Capacitor Cm (10pF) and resistor Rm (1MΩ) represent the static membrane capacitance and resistance. Depending on the state of the two analog switches, SW1 and SW2, either capacitor Cv1 or Cv2 is put in parallel with Cm to create the overall membrane capacitance. The microcontroller (PIC18F4525, Microchip, Chandler, AZ) is programmed to output driving signals RC1 and RC0 to control the analog switches SW1 and SW2 respectively, as shown in Figure 1B. Their always inverse phases assures only one of the switches is closed at any moment so that only one of the capacitors, Cv1 or Cv2, is included in the membrane capacitance. If there is any difference between these two capacitors, it will manifest itself as overall membrane capacitance change. As a matter of fact, the capacitance change does not only attribute from the capacitors Cv1 and Cv2, but also from all the other elements along these two circuit branches, such as the switches. So it is a lump-sum capacitance difference between these two branches, though Cv1 and Cv2 provide the largest portion of it. To achieve as small as tens of fF capacitance change, Cv1 and Cv2 are actually implemented with an assembly of standard 4.7 pF (±10%) porcelain capacitors. Although these capacitors all have the same nominal values, inherent manufacture errors make their actual values deviate from the standard value to different degrees. This deviation is stated in the product specifications, such as 10%. So, if two capacitors are randomly picked, their capacitance will be different, but the difference is small relative to their nominal value. For example, if the nominal value is 4.7pF and error tolerance is 10%, the difference between two capacitors would be in the range of hundreds of fF. Furthermore, if multiple capacitors in series are treated as one capacitor, the capacitance change would drop to the range of tens of fF. Thus, it is possible to achieve different levels of capacitance changes by picking different capacitors and using different numbers of capacitors in series.

The switches SW1 and SW2 are controlled by the microcontroller, so, by reprogramming it, different control patterns, or the resulting membrane capacitance change patterns, can be achieved. For example, the frequency of RC0 and RC1 will determine how often the capacitance changes,

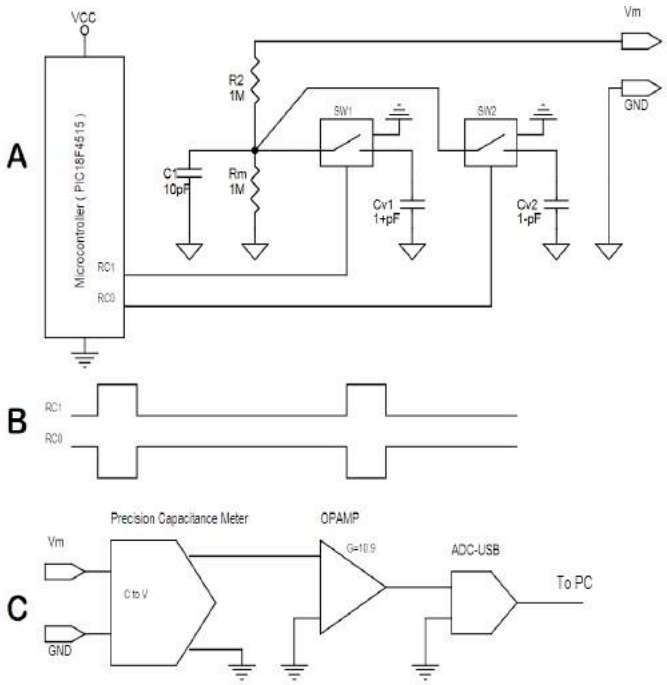

Fig. 1. Schematic and testing circuit of electronic cell membrane model.

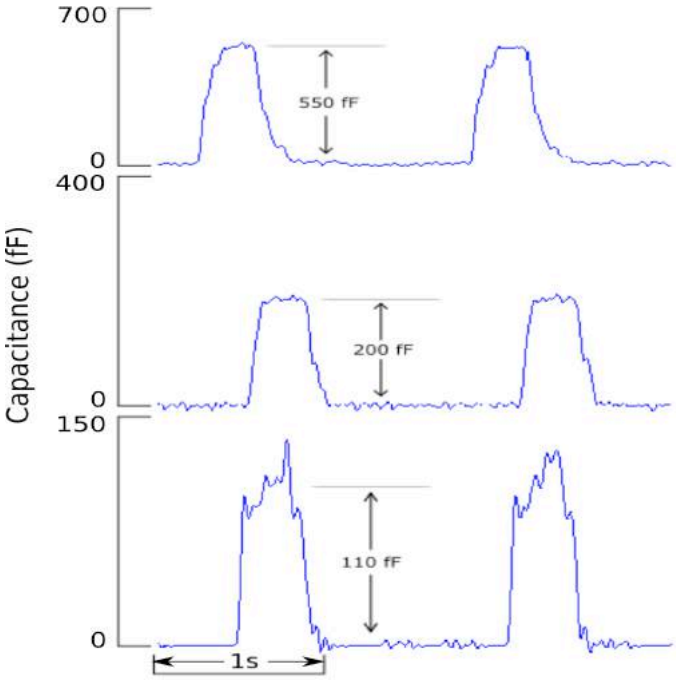

Fig. 2. Outputs from the precision capacitance meter outputs with different capacitance changes.

and the duty cycle will determine duration of each capacitance value, as shown in Fig. 1B.

B. Testing

To verify the behavior of this model, a precision capacitance meter (Model 3000, GLK Instruments, San Diego, CA) is used, as shown in Fig. 1C. It accepts the lead capacitor and outputs an analog voltage proportional to the capacitance value. A capacitance of 20 pF will result to a voltage output of 200 mV. In order to record measurements, an Analog to Digital Converter (USB-1208FS, Measurement Computing, Norton, MA) is used to sample the output of capacitance meter and upload the digital data to a PC. An op-amp provides a gain of 10.9 to scale up the capacitance meter output so as to make better use of the ADC dynamic range. On the PC side, sample data is collected and viewed using the software Instacal® and TracerDAQ® (Measurement Computing, Norton, MA).

III. Results

By using three configurations for both capacitance branches, three values of cell capacitance change were recorded with 1 KHz sampling rate for a 15s duration, as shown in Fig. 2. The duty cycle of the vesicle capacitance pulses was set to 0.5 s due to the limited speed of the capacitance meter. Achieved capacitance change values were 550 fF, 200 fF, and 110 fF from top to bottom, and Cv1/Cv2 configurations were single capacitor, four capacitors in series, and ten capacitors in series, respectively. Attempts were made to further reduce the capacitance change by increasing the number of capacitors, but without success due to the noise floor of the testing equipment.

IV. Discussion

This project successfully implemented an electronic model for simulating the dynamic changes of cell membrane capacitance due to vesicle transportations. By switching between two branches of series-connected capacitors, small differential capacitance changes on the order of 10-100 fF were achieved by using standard capacitors on the order of 1 pF. For future work, more switched capacitor branches will be added and calibrated to achieve multi-level capacitance changes. This instrument will be used for the development of digital detection algorithms capable of the fF accuracy with a time resolution on the order of 1 ms.

Acknowledgements

The authors would like to thank the University of Rhode Island Undergraduate Research Initiative Awards Program for recognizing and funding this project. This work was also supported by a NIH SBIR grant (No. 1R43NS087659-01A1).

References

[1] Schweizer, F. Capacitance measurements. http://schweizerlab.org/capacitance-measurements, 2013.

[2] Lempka, S. F., and D. W. Barnett. Optimization of multi-frequency techniques used for cell membrane capacitance estimation. 26th Ann. Int. Conf. IEEE EMBS, San Francisco, CA, USA, pp. 522-525, 2004.

[3] Misler, S., and D. W. Barnett. An optimized approach to membrane capacitance estimation using dual-frequency excitation. *Biophys J*. vol. 72, pp. 1641-1658, 1997.

[4] Holevinsky, K. O., and Nelson, D. J. Membrane capacitance changes associated with particle uptake during phagocytosis in macrophages. *Biophysical Journal*, vol. *75*(5), pp. 2577-2586, 1998.

[5] Cullen, J., P. Patel, J. Shannon, E. Chabot, and Y. Sun. Instrumentation for cell capacitance measurements: switching sinusoidal excitations for studying cell membrane transport. 40th Ann. Northeast Bioengineering Conference, Boston, MA, April 25-27, 2014.

An Electronic Neuron Emulator that Models Inward and Outward Membrane Currents

Kimberly Hoffman, Vi Tran, Jessica Blandin, Jiang Wu, Ph.D., and Ying Sun, Ph.D.
Department of Electrical, Computer and Biomedical Engineering, University of Rhode Island,
4 East Alumni Avenue, Kingston, RI, 02881, USA. Correspondence email: yingsun@uri.edu

***Abstract*—The purpose of the project was to design an electronic neuron emulator capable of producing inward and outward currents similar to potassium and sodium voltage gated channels found in a cell membrane. The design employed novel capacitance sources outputting controlled amounts of charges suitable for testing instruments such as the patch clamp amplifier. To generate an action potential, two pre-charged capacitors representing the inward and outward currents were momentarily cascaded on to a resistor-capacitor circuit representing the cell membrane via analog switches. Under the control of an embedded microprocessor, the action potentials were fired in a rate responsive way according to the resting membrane potential. The resulting neuron emulator should be useful for testing neuroscience instruments, teaching electrophysiology, and studying mechanisms of ionic channels.**

Keywords—electronic neuron emulator; inward and outward currents; capacitance source; embedded system

I. Introduction

The landmark study by Hodgkin and Huxley [1] unveiled the essential properties of the ionic currents that propagate during a neuronal action potential. In an excitable cell, the interaction between the fast inward sodium current and the slow outward potassium current results in the firing of an action potential. However, the Hodgkin-Huxley model characterized by four nonlinear, time-varying differential equations is difficult to implement in an electronic neuron emulator intended for real-time interactive operations. This project aims to design a neuron emulator that is able to reproduce rate responsive action potentials but still retains a representation of the underlying mechanisms of ionic currents. The circuit design is based off a previous neuron emulator that uses a pre-charged capacitor as the source instead of either a voltage source or a current source [2]-[4]. The new focus in this study is on the shaping of the action potential by controlling the interaction between the inward current and the outward current. In addition, the firing of the action potentials is programmed to be rate responsive according to the resting membrane potential, thereby allowing for interaction with an external stimulation.

II. METHODS

A. Hardware

As shown in Fig. 1A, the passive electrical properties of the neuronal cell membrane are represented by Rm and Cm. The inward current and the outward current are generated with capacitors Cin and Cout, respectively, pre-charged to the appropriate voltages. The generation of action potentials is done by changing the circuit topology dynamically via a set of

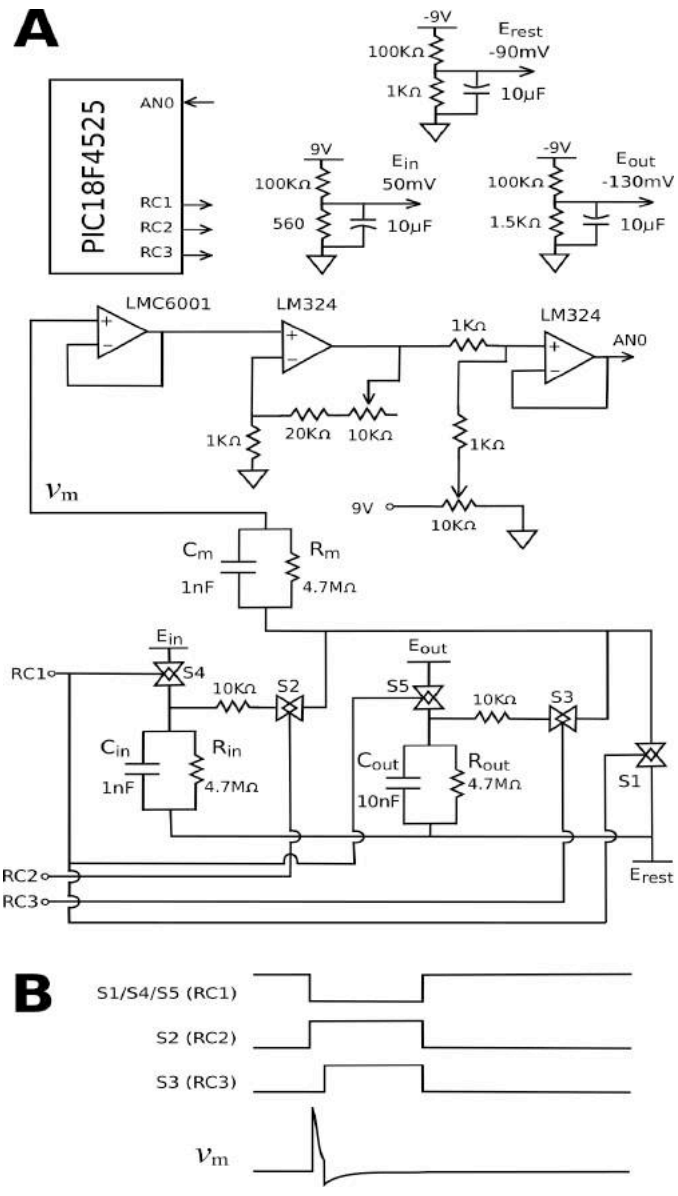

Fig. 1. Panel A: schematic diagram of the neuron emulator; Panel B: timing for the switches and the desired action potential (vm) waveform.

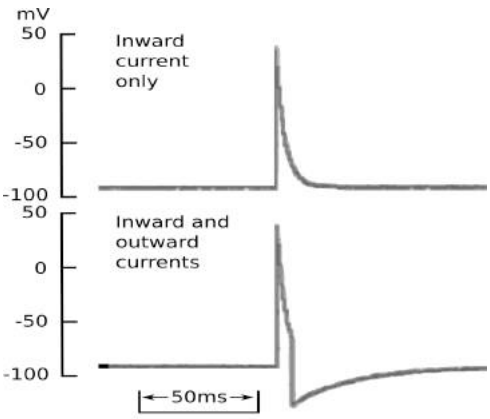

Fig. 2. Action potential waveform with inward current only (top) and with both inward current and outward current (bottom).

analog switches (S1-S5, MC14066). Before firing, the Rm-Cm unit is connected to the resting potential Erest via switch S1. Switches S4 and S5 are synchronized with S1 to pre-charge Cin and Cout. To initiate an action potential, the fast inward current is injected by activating S2 and deactivating S1, S4 and S5 at the same time. After a short delay (such as 10 ms) the slow outward current is injected by activating S3. The membrane potential (vm) is monitored by an embedded microprocessor (PIC18F4515, Microchip, Chandler, AZ). To minimize the loading effect, an OP amp with ultra-low input current (LMC6001) is used to measure the voltage (vm) at the Rm-Cm unit. The signal is amplified by additional OP amps (LM324) before it is acquired by the on-chip analog-to-digital converter of the microprocessor via input AN0.

B. Software

The microprocessor implements a customized software developed in the C++ language using MPLab X (Microchip, Chandler, AZ). Fig. 1B shows the timing of the I/O lines RC1-RC3 that control the switches (S1-S5). The desirable waveform of the action potential (vm) contains an initial spike from the fast inward current followed by a hyperpolarization from the slow outward current. The hyperpolarization period last for 160 ms before switching back to the resting membrane potential. The resting membrane potential is monitored by the processor to determine the firing rate of the next action potential. An empirical relationship is implemented to make the firing interval inversely proportional to the resting potential.

III. Results

Fig. 2 shows an action potential generated by the neuron emulator with the inward current only (top) and with both the inward current and the outward current (bottom). The slow outward current was responsible for creating the hyper-polarization phase typically observed in a live neuron. Figure 3 shows an episode of continuous firing of action potentials in a rate responsive way. The resting membrane potential was raised to simulate an external stimulation such as a current clamp. The neuron emulator responded by increasing the firing rate in accordance with the resting membrane potential.

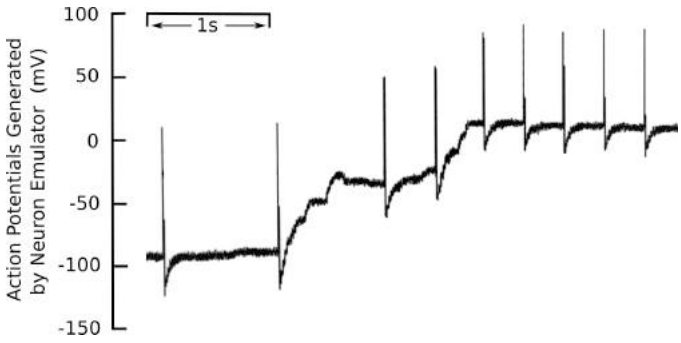

Fig. 3. As the resting membrane potential was raised, the neuron emulator fired action potentials in a rate-responsive way by increasing the firing rate accordingly.

IV. Discussion

The electronic neuron emulator developed in this project has the following advantages. First, it represents the passive electrical properties by setting the appropriate membrane resistance and capacitance (Rm and Cm) and a realistic resting membrane potential (Erest). Second, it generates an action potential of a realistic waveform including a depolarization phase and a hyperpolarization phase. Third, the interaction between the fast inward current and the slow outward current is modeled to reflect the underlying mechanisms of ionic channels. Fourth, the rate responsive nature of a live neuron is represented such that the neuron emulator interacts with an external stimulation by adjusting its rate of firing the action potentials.

Future work includes further testings of the neuron emulator with electrophysiological instruments such as current clamp, voltage clamp, dynamic clamp, and patch clamp [5]. In addition, a graphic user interface will be added to provide control and waveform display capabilities by using a handheld device via a Bluetooth wireless link.

Acknowledgment

This work was supported by a grant from the University of Rhode Island 2015-2016 Undergraduate Research Initiative Awards program and a SBIR grant from the National Institutes of Health (No. 1R43NS087659-01A1).

References

[1] Hodgkin, A. L., and A. F. Huxley. "A quantitative description of membrane current and its application to conduction and excitation in nerve." J. Physiol. 117(4): 500–544, 1952.

[2] Wu, Y. C., J. Y. Chen, R. Rieger, and Y. Sun. “A neuron emulator for single-electrode settings.” 37th Annual Northeast Bioengineering Conference, Rensselaer Polytechnic Institute, Tory, NY, 2011.

[3] Ausfresser, G., and Y. Sun. “Neuron emulation, instrumentation, and communication for a neuroscience instrument.” 38th Northeast Bioengineering Conference, Philadelphia, PA, pp. 259-260, 2012.

[4] Sun, Y., and R. Rieger. “Apparatus for memristor/neuron emulation and testing.” U.S. Patent 8,990,137 B2, March 24, 2015.

[5] Sun, Y., J. Wu, L. Collis, and R. B. Hill. “Apparatus for neuromuscular measurement and control.” US Patent No. 7,489,965 B2, February 10, 2009.

An Activity Analyzing System for Elders Based on Standalone Embedded Image Platform

Jesse McVaney, Victoria Danielson, Shane Ramos, Dr. Jiang Wu, and Dr. Ying Sun
Department of Computer, Electrical, and Biomedical Engineering
The University of Rhode Island, Kingston, Rhode Island

***Abstract*— In this project, a standalone embedded image processing system, or Activity Analyzing System (AAS), is developed to monitor and analyze the activities of elderly patients living independently. Built upon the Blackfin Low Power Image Platform (BLIP), it captures and processes images locally and in real-time to identify the activities of patients through motion detection within regions of interest. The activity metadata can be used for family care and medical purposes. The system can be set up to automatically trigger an alarm in case of such emergency as sudden-fall. It can also serve as a reminder for medicine taking, sleeping, daily exercise, etc.**

Keywords – image processing, embedded system, elder monitoring, activity analysis.

I. Introduction

Families with elderly patients living independently are always worrying if their elders are sleeping well, getting out of bed at a reasonable time, eating properly, taking their medication at the correct times, etc., since they cannot constantly watch them. Inactivity of elderly patients can cause pulmonary and respiratory complications [1]. Monitoring medication intake is crucial for elderly patients diagnosed with Alzheimer's or Dementia; it is not uncommon for those to forget to take their medication, or take more than the recommended dose. A constant observation becomes necessary for a better life of the elders.

The new emerging technology in real-time image/video processing and communication provides a feasible and non-invasive solution to the above requirements. Many monitoring/surveillance products were brought to market based on this concept. However, most of these available systems, such as the AvaSure and ATVideo systems, take a centralized approach, which captures images on patient's premises and then transmits them to a control center. At the control center, the images are either watched by trained observers or redirected to mobile devices of the patient family for observation. Sometimes they are further processed by powerful central computers as auxiliary help to observers. In this approach, the communication and observation requirement add significant operation costs and response time.

To overcome the drawback of centralized approach, a distributed approach is preferred, which captures and analyzes images both in real-time and locally at the patient's site; resulting in lower cost and shorter response time. The recent embedded processors, such as the Blackfin embedded processors of Analog Devices Inc., equipped with greatly improved computation power, full integration of image sensor interface, and ready-to-use image processing libraries makes this approach possible.

In this project, the distributed approach is taken and an AAS was developed using the BLIP as the image capturing and computing hardware. An image processing software framework is created, in which a variety of image analyzing modules can be developed. As one example, a region-of-interest (ROI) based motion detection algorithm was designed and implemented. The results show the feasibility of the distributed approach and the great potential of this hardware platform and software framework.

II. Methods

A. Hardware

The hardware platform of AAS is the BLIP development board (by Analog Devices Inc.). It provides the necessary computing power with its on-board ADSP-BF707 embedded processor (operating at speeds up to 400MHz core frequency), 2GB SDRAM memory, and 32MB flash memory [2]. The image capturing capability is achieved with an on-board image sensor (Aptina ASX340) which can supply a stream of images of 640 by 480 resolution at a frame rate of 30 fps. In addition, the BLIP board integrates a plethora of peripheral interfaces, such as SPI, I2C and USB, for easy connection to different sensors, wireless communication modules, storage, and digital-controlled actuators. The AAS system is set up, as shown in Figure 1, to use one of the USB ports as an upload link to a PC. This USB link is used solely for demonstrating the image analyzing performance while the processor carries out all the analyzing tasks without any interference from other outside components.

The compact size (2.5" by 3.5") of the BLIP makes it suitable to be a portable device that can be easily installed at patients' homes.

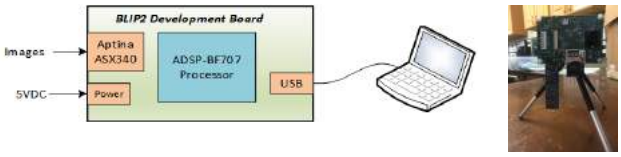

Figure 1: AAS System Setup

B. Software

The software of the AAS was developed with Cross Core Embedded Studio and software component library of BLIP, including image sensor drivers, USB drivers, image processing library, and board supporting package. The ICE-1000 emulator is used to download the developed software to the BLIP and debug during development. The onboard flash memory holds the final product software.

C. Algorithm

A region-based motion detection algorithm was developed. The ROIs were pre-defined to indicate the image areas, which are related to the monitoring purposes. For example, a medicine cabinet area can be used for determine whether or

not the patient is taking their medication and at what times. The motion will indicate the patient's activity in the regions.

This project took a similar approach as the AIMS algorithm. The algorithm uses a pixel-wise difference between two adjacent image frames as the cue of motion [3]. The existence of motion at a particular pixel is identified when the luminance difference of the pixel in two image frames is larger than a pre-defined threshold, or

$$|I_{k+1}(x,y) - I_k(x,y)| > d \quad (1)$$

where $I_{k+1}(x,y)$ and $I_k(x,y)$ are the luminance at the pixel (x,y) in $(k+1)^{th}$ and k^{th} frame respectively, and d is the pre-defined or adaptive threshold.

The image sensor interface, Enhanced Peripheral Parallel Interface (ePPI), of ADSP-BF707 continuously stores the raw image frame data from the image sensor into two pre-allocated memory areas alternatively, or ping-pong. The two-dimensional image frames are mapped in one-dimensional contiguous memory. This mapping relation can be formulated as

$$x = i \bmod 640,\ y = (i-x)/640 \quad (2)$$

where x and y are the coordinates in image frame of the i^{th} pixel in frame memory, and the image frame is assumed to be 640 pixels wide.

A ROI was defined with its upper left corner, width, height, Boolean motion flag, and minimum object size. This allows a region to be easily created at a specific spot in the frame with adjustable width and height various situations. The Boolean flag remains false until an object passes within the ROI and meets the minimum object size threshold. The object size is determined by counting the number of detected motion pixels within the ROI. When the minimum object size threshold is met, the Boolean flag will be evaluated as true. Figure 2 shows the flowchart of this processing procedure.

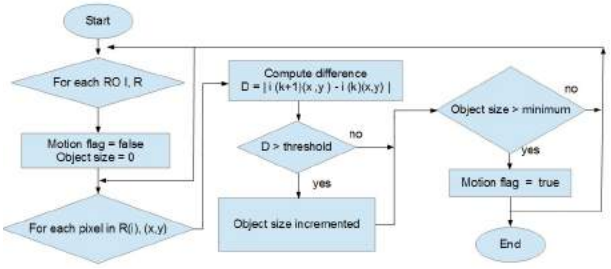

Figure 2: Region-based Motion Detection Algorithm

III. Results

To demonstrate the performance of this AAS, one of the USB ports of the BLIP board was used to upload real-time processed black-white images to PC for display. The algorithm generates these images by assigning the value 255 and 0 to motion and motionless pixels respectively. A visual flag is drawn on the frames at the upper right corner to indicate detected motions in the ROIs.

Two scenarios of motion detection are shown in Figure 4, where the region of interest is defined as a 50 pixels by 50 pixels region with upper left coordinate at the center of the frame. In Figure 3A, the subject's moving hand was detected outside of the region, and no motion flag was triggered at the upper right corner. However, in Figure 3B, where the subject moved his hand into the region of interest, the motion flag was successfully triggered and was visually drawn at the upper right corner of the frame.

A B

Figure 3: (A) Object outside ROI, (B) Object inside ROI

IV. Discussion

The main focus of this project was to develop a combined hardware and software image based embedded platform to easily monitor and analyze the activities of elderly patients. This platform has vast potential to address many other demands, such as fall detection, though only simple motion detection was implemented in this project. Future creative developments made to this system can reduce the costly need to place elderly patients in a nursing/assisted living home or to hire a visiting nurse, while making the patient's families feel comfortable leaving them alone.

The region-based motion detection algorithm developed in this project can still be further expanded to trigger alert of certain events, including entry and exit of areas in hospitals/ nursing homes, medication and food intake areas, and restroom. Furthermore, activity patterns could also be logged over extended periods. For example, a ROI could be defined for a sleeping area where restless activity could be logged when motion is detected. This has applications not only for sleep quality but also for deviation from normal activity patterns, such as sleeping patterns. Furthermore, the rich peripheral interfaces of BLIP allow for many other novel uses, such as wireless communication, appliance control, and so on.

Many people have elderly family members suffering from Dementia and Alzheimer's, and so need constant monitoring and care, including members of this project team. This imminent requirement ignited the passion and motivation of the team for this project.

Acknowledgment

The authors would like to express their gratitude to the University of Rhode Island Undergraduate Research Initiative Awards Program for recognizing and funding this project, and Analog Devices Inc. for donating the BLIP development boards.

Reference

1. Troosters, Thierry, "Physical Inactivity in Patients with COPD, a Controlled Multi-center Pilot-study." Respiratory Medicine 104.7 (2010): 1005-011.
2. ADZS-BF707-BLIP2 Board Evaluation System Manual, Revision 1.0 Analog Devices, Inc. Norwood, MA: Analog Devices, Inc. (2015).
3. Han, Xu. "Active Motion Image Seeking (AIMS) Camera System." (2002): 4+. Master Thesis: Department of Computer, Electrical, and Biomedical Engineering, The University of Rhode Island. Web.